Atmos. Chem. Phys. Discuss., 15, 27943–28004, 2015
www.atmos-chem-phys-discuss.net/15/27943/2015/
doi:10.5194/acpd-15-27943-2015

Atmospheric Chemistry and Physics Discussions

Polly^{NET}: a global network of automated Raman-polarization lidars for continuous aerosol profiling

H. Baars[1], T. Kanitz[1,a], R. Engelmann[1], D. Althausen[1], B. Heese[1], M. Komppula[2], J. Preißler[4,b], M. Tesche[7,c], A. Ansmann[1], U. Wandinger[1], J.-H. Lim[5], J. Y. Ahn[5], I. S. Stachlewska[6], V. Amiridis[8], E. Marinou[8,21], P. Seifert[1], J. Hofer[1], A. Skupin[1], F. Schneider[1], S. Bohlmann[1], A. Foth[1,16], S. Bley[1], A. Pfüller[2,†], E. Giannakaki[2], H. Lihavainen[3], Y. Viisanen[3], R. K. Hooda[3,12], S. Pereira[4], D. Bortoli[4], F. Wagner[4,20], I. Mattis[20], L. Janicka[6], K. M. Markowicz[6], P. Achtert[7,d], P. Artaxo[9], T. Pauliquevis[10], R. A. F. Souza[11], V. P. Sharma[12], P. G. van Zyl[13], J. P. Beukes[13], J. Y. Sun[14], E. G. Rohwer[15], R. Deng[17], R. E. Mamouri[18], and F. Zamorano[19]

[1]Leibniz Institute for Tropospheric Research, Permoserstraße 15, 04318 Leipzig, Germany
[2]Finnish Meteorological Institute, Kuopio, Finland
[3]Finnish Meteorological Institute, Helsinki, Finland
[4]Évora University, Institute for Earth Sciences, Évora, Portugal
[5]National Institute of Environmental Research, Incheon, Republic of Korea
[6]Institute of Geophysics, Faculty of Physics, University of Warsaw, Warsaw, Poland

[7]Department for Environmental Science and Analytical Chemistry, and Department of Meteorology, Stockholm University, Stockholm, Sweden
[8]IAASARS, National Observatory of Athens, Athens, Greece
[9]Institute of Physics, University of São Paulo, São Paulo, Brazil
[10]Department of Biological Sciences, Federal University of São Paulo at Diadema, Diadema, Brazil
[11]Coordination of Meteorology, University of the State of Amazonas, Manaus, Brazil
[12]The Energy and Resources Institute, New Delhi, India
[13]Unit for Environmental Sciences and Management, North-West University, Potchefstroom, South Africa
[14]Key Laboratory of Atmospheric Chemistry of CMA, Institute of Atmospheric Composition, Chinese Academy of Meteorological Sciences, Beijing, China
[15]Physics Department, Stellenbosch University, Stellenbosch, South Africa
[16]Leipzig Institute for Meteorology, University of Leipzig, Leipzig, Germany
[17]School of Geography and Planning, Sun Yat-sen University, Guangzhou, China
[18]Cyprus University of Technology, Department of Civil Engineering and Geomatics, Limassol, Cyprus
[19]Laboratory of Atmospheric Research, University of Magallanes, Punta Arenas, Chile
[20]Hohenpeißenberg Meteorological Observatory, Deutscher Wetterdienst, Hohenpeißenberg, Germany
[21]Laboratory of Atmospheric Physics, Aristotle University of Thessaloniki, Thessaloniki, Greece
[a]now at: European Space Agency, ESTEC, Noordwijk, the Netherlands
[b]now at: Centre for Climate and Air Pollution Studies, School of Physics, National University of Ireland Galway, Galway, Ireland
[c]now at: School of Physics, Astronomy and Mathematics, University of Hertfordshire, Hatfield, UK
[d]now at: School of Earth and Environment, University of Leeds, Leeds, UK
[†]deceased

ACPD
15, 27943–28004, 2015

Received: 10 August 2015 – Accepted: 20 September 2015 – Published: 15 October 2015

Correspondence to: H. Baars (baars@tropos.de)

Published by Copernicus Publications on behalf of the European Geosciences Union.

Abstract

A global vertically resolved aerosol data set covering more than 10 years of observations at more than 20 measurement sites distributed from 63° N to 52° S and 72° W to 124° E has been achieved within the Raman and polarization lidar network Polly^{NET}. This network consists of portable, remote-controlled multiwavelength-polarization-Raman lidars (Polly) for automated and continuous 24/7 observations of clouds and aerosols. Polly^{NET} is an independent, voluntary, and scientific network. All Polly lidars feature a standardized instrument design and apply unified calibration, quality control, and data analysis. The observations are processed in near-real time without manual intervention, and are presented online at http://polly.tropos.de. The paper gives an overview of the observations on four continents and two research vessels obtained with eight Polly systems. The specific aerosol types at these locations (mineral dust, smoke, dust-smoke and other dusty mixtures, urban haze, and volcanic ash) are identified by their Ångström exponent, lidar ratio, and depolarization ratio. The vertical aerosol distribution at the Polly^{NET} locations is discussed on the basis of more than 55 000 automatically retrieved 30 min particle backscatter coefficient profiles at 532 nm. A seasonal analysis of measurements at selected sites revealed typical and extraordinary aerosol conditions as well as seasonal differences. These studies show the potential of Polly^{NET} to support the establishment of a global aerosol climatology that covers the entire troposphere.

1 Introduction

Aerosol particles have been depicted as one important and underdetermined component that affects the Earth's energy budget. Their complex nature regarding size, shape, and chemical composition, their highly variable temporal and spatial distribution in the atmosphere, and their complex interactions with clouds require strong effort in their observation and characterization (IPCC, 2014; Stevens and Feingold, 2009).

ACPD
15, 27943–28004, 2015

In addition, the volcanic eruption hazards of Eyjafjallajökull and Grimsvötn for aircraft safety in Europe have shown the need for near-real-time information of height-resolved aerosol concentration on continental scales.

Lidars are a key instrument for the characterization of aerosols and their impact on the Earth's environment as they are able to provide vertically resolved information of aerosols. With multiwavelength-Raman-polarization lidars, aerosol layers can be characterized in terms of types, size distribution, and concentration (Ansmann and Müller, 2005; Müller et al., 2007; Ansmann et al., 2012).

As a global coverage of height-resolved aerosol monitoring is strongly needed, either space-borne lidars, e.g., CALIOP (Cloud–Aerosol Lidar with Orthogonal Polarization) aboard the polar-orbiting CALIPSO satellite (Cloud–Aerosol Lidar and Infrared Pathfinder Satellite Observation, Winker et al., 2009) or ground-based networks of ceilometers, micro-pulse lidars, or scientific Raman lidars are applied (Bösenberg et al., 2007; Hoff and Pappalardo, 2010). The shortcomings of the space-borne lidar CALIOP are the need for a priori information of aerosol type to retrieve particle backscatter coefficient profiles and the low temporal resolution, because it overpasses the same area only every 16th day. Ceilometer (e.g., Flentje et al., 2010) and micro-pulse lidar (Welton et al., 2001) networks are operated 24/7 at many locations world wide but are not able to distinguish aerosols in terms of their size distribution, shape, or extinction efficiency, and thus their type (Spinhirne et al., 1995; Heese et al., 2010; Stachlewska et al., 2012).

Within EARLINET, the European Aerosol Research Lidar Network[1] (Pappalardo et al., 2014), aerosol profiling and characterization is performed within Europe by different Raman and polarization lidars three times per week. EARLINET members have developed lidar techniques and algorithms in order to harmonize the lidar measurements, to setup quality standards, to perform systematic test routines, and to improve the lidar data evaluation. However, most of the lidar systems are prototypes leading to a huge variety of partly manually controlled system setups. Similar limitations hold

[1]Now part of the Aerosols, Clouds, and Trace gases Research InfraStructure (ACTRIS).

ACPD
15, 27943–28004, 2015

for the American Lidar Network ALINE (Antuña et al., 2012; Barbosa et al., 2014) and the Commonwealth of Independent States Lidar Network CISLiNet (Chaikovsky et al., 2006). Within the Asian Dust Network (AD-NET, Sugimoto et al., 2008), standardized lidar instruments, mostly with 2-wavelength backscatter (at 532 and 1064 nm) and 1-wavelength depolarization (at 532 nm) capabilities, are applied and the attenuated backscatter coefficients and the volume depolarization ratio are automatically retrieved. At the six primary stations also Raman capabilities are available (Sugimoto et al., 2014). The network is however limited regionally to the Asian dust belt.

Motivated by the urgent need for robust multiwavelength-Raman-polarization lidars that are easy to operate and allow aerosol typing, a portable lidar system, called Polly^{XT}, has been developed at the Leibniz Institute for Tropospheric Research (TROPOS) with international partners during the last decade (Althausen et al., 2009; Engelmann et al., 2015). The aim was to develop a sophisticated multiwavelength-Raman-polarization lidar for scientific purpose, but with the advantages of an easy-to-use and well-characterized instrument with same design, same automated operation, and same centralized data processing in line with the CIMEL Sun photometer of AERONET (Holben et al., 2001). These Polly systems have been developed for continuous, standalone operation in remote environments and were successfully deployed in the high northern latitudes of Finland (> 30 cm snow and $< -20\,^{\circ}$C, Hirsikko et al., 2014), in the rain forest of the Amazonian Basin with temperatures of $> 30\,^{\circ}$C and high relative humidity (Baars et al., 2012), and under permanent mechanical stress from motor vibrations plus rough sea aboard the research vessel *Polarstern* (Kanitz et al., 2013a).

As the number of Polly systems and measurement sites has increased with time, an independent, voluntary, international network of cooperating institutes, the so-called Polly^{NET} (Althausen et al., 2013), has evolved. Namely the Finnish Meteorological Institute (FMI), the National Institute of Environmental Research (NIER) in Korea, the Évora University in Portugal (UE-ICT), the University of Warsaw (UW) in Poland, and the National Observatory of Athens (NOA) in Greece contribute actively, i.e. host Polly

ACPD
15, 27943–28004, 2015

systems, to the network. Each group contributes with its expertise and knowledge to the network and to joint scientific projects.

Polly lidar measurements have been performed at more than 20 locations in Europe, the Amazon rain forest, Southern Chile, South Africa, India, China, Korea, and over the Atlantic Ocean and very different aerosol types and aerosol mixtures could be observed. Figure 1 shows the locations of the six stationary[2] plus one mobile long-term (green color), and the 14 temporary (red color) measurement sites within Polly^{NET}. In addition, typical aerosol types and their transport paths are indicated.

Data from the permanent locations as well as from the measurement campaigns are centrally collected via internet, processed, and displayed in near-real time. This near-real-time processing ensures a fast system control (instrument monitoring) and a first quality assurance by all partners.

First automated data analysis routines for Polly were developed to determine the top height of the planetary boundary layer (PBL, Baars et al., 2008). However, the automated analysis of highly sophisticated multiwavelength-Raman-polarization lidar measurements with respect to vertical profiles of aerosol optical properties was missing. Based on achievements within the development of the Single Calculus Chain of EARLINET (D'Amico et al., 2015), but extended for an autonomous near-real-time analysis of continuous measurements around the globe, an automatic data processing chain for the retrieval of aerosol optical properties has been developed thanks to the advantage of the unified Polly family design. With this processing chain, data from the Polly^{NET} lidars is screened for appropriate weather conditions and profiles of the particle backscatter coefficient (355, 532, and 1064 nm), the particle extinction coefficient (355 and 532 nm), and the particle depolarization ratio (532 nm) are obtained and presented online.

In doing so, an aerosol climatology of the vertical aerosol distribution and of aerosol-type-dependent parameters like the lidar ratio (extinction-to-backscatter ratio), the Ångström exponent, and the particle linear depolarization ratio has evolved and is

[2]The four European stationary measurement sites belong to EARLINET.

ACPD
15, 27943–28004, 2015

presented in this paper. This database might be a valuable tool for space-borne lidar missions like CALIPSO or the upcoming ADM-Aeolus (Atmospheric Dynamics Mission, Stoffelen et al., 2005) and EarthCARE (Earth Clouds, Aerosols and Radiation Explorer, Illingworth et al., 2015) missions. The findings may also serve for the verification of aerosol transport models (e. g., Binietoglou et al., 2015; Haustein et al., 2009) or support studies on the radiative impact of aerosol layers on the Earth's energy budget (e.g., Kanitz et al., 2013b). Thus, Polly^{NET} can give a valuable contribution to the understanding of the complex nature of atmospheric particles which is a prerequisite to understand their complex interactions with clouds.

The paper is structured as follows: Sect. 2 gives a brief introduction into the Polly systems. In Sect. 3, the different measurement locations are introduced and the main findings of more than 10 years of Polly observations are summarized providing an overview of aerosol-type-dependent properties observed within Polly^{NET}. Section 4 presents the data analysis algorithm, which is explained in more detail in the Appendix A. The applicability and potential of the automated algorithm for the Polly systems is discussed for one example case of a Saharan dust event observed at Leipzig in 2012 (Sect. 5). In Sect. 6, the currently most comprehensive harmonized aerosol information from ground-based lidars worldwide is presented based on the automatically analyzed global data set of Polly^{NET}. At the end of the paper, a conclusion and future plans are given.

2 The Portable Lidar Polly

The first Polly system (Althausen et al., 2009) is a one-wavelength Raman lidar at 532 nm with an emitted laser energy of 120 mJ and a primary mirror of 20 cm in diameter. Data is acquired with 37.5 m vertical resolution and averaged over 450 shots (15 Hz laser frequency). Figure 2 shows the first profiles of the backscatter and extinction coefficients measured by Polly on 10 December 2002 in Leipzig, Germany. The backscatter coefficient is 10 M m^{-1} sr^{-1} in the boundary layer that extended up to

ACPD
15, 27943–28004, 2015

about 350 m height. Optically thin, lofted layers were present between 700 and 1100 m height. While the first measurement lasted only about 24 min, this system was continuously improved for automatic operation and now runs unattended in 24/7[3] mode. The latest developed Polly^{XT} (with extended capabilities) is a so-called 3 + 2 + 2 + 1 + 1 + 1[4] Raman, polarization, and water-vapor lidar with near-range capabilities. This system emits light at 1064, 532, and 355 nm at an energy of 180, 110, 60 mJ. The receiver unit consists of a primary mirror of 30 cm in diameter. With this setup the backscatter coefficient at 1064, 532, and 355 nm, and the extinction coefficient at 532 and 355 nm can be determined. Thus, aerosols can be characterized by their lidar ratio and Ångström exponent (Müller et al., 2007), but also in terms of microphysical properties and the single scattering albedo (e. g., Ansmann and Müller, 2005). In addition, two polarization-sensitive channels allow the determination of the particle linear depolarization ratio (Freudenthaler et al., 2009) at 355 and 532 nm providing information on the shape of the scatterer. With this information, e.g., mixed-dust layers can be analyzed for the fractions of pure dust and other aerosol types (Tesche et al., 2011; Baars et al., 2012; Kanitz et al., 2013a). Vertical profiles of aerosol properties up to 20 km height can be derived with this receiver unit. Additionally, profiles of the water-vapor mixing ratio can be determined via the measurement of the inelastic water-vapor backscatter at 407 nm wavelength (Reichardt et al., 2012; Foth et al., 2015). Below about 600–800 m a.g.l. (above ground level), the overlap of the laser beam and the receiver field of view is incomplete and needs to be corrected (e.g., with the methodology described by Wandinger and Ansmann, 2002). As a consequence, a second detection unit together with a near-range telescope was added to the system to detect the elastic and inelastic backscatter at 532 and 607 nm in the lowermost height range above the system. As a result, the determined overlap function of the far-range channels can be verified and backscatter and extinction profiles can be obtained down to about 100 m a.g.l. The data

[3]Continuously 24 h a day, 7 days per week.

[4]3 elastic, 2 Raman, 2 depolarization, 1 water-vapor, 1 near-range elastic, and 1 near-range Raman signals.

ACPD
15, 27943–28004, 2015

of all channels is acquired with a vertical resolution of 7.5 m in temporal steps of 30 s (laser frequency 20 Hz). Further system details are given by Althausen et al. (2009) and Engelmann et al. (2015).

By the end of the year 2014, eight Polly systems have been developed and employed. All these lidars differ slightly from each other as the capabilities have continuously expanded from the very first Polly version to the latest extended version. Nevertheless, they feature a similar design, the same data format, and benefit from unified calibration and quality assurance routines. An overview of the different systems including their capabilities and different characteristics can be found in Engelmann et al. (2015).

3 Global measurement locations and published results of Polly^{NET}

The Polly systems have been deployed for vertical profiling of aerosols and clouds at measurement sites from 64° N to 53° S and from 71° W to 125° E. This includes areas with Arctic conditions in Finland (63° N, 27° E), tropical conditions in the Amazon basin (3° S, and 60° W), and the Antarctic regime at the southern peak of South America at Punta Arenas (53° S, 71° W). Notable measurement sites are the two research vessels *Meteor* and *Polarstern*, which allow longitudinal and latitudinal cross section observations along the Atlantic (Kanitz et al., 2013a, 2014b). Details on the position and the measurement periods of each station as well as the number of measurement days by the end of 2014 are given in Table 1.

The global distribution of the measurement stations allows the characterization of the main aerosol types, i.e., the aerosol types used for the measurements of the space-borne lidar CALIOP (clean continental, polluted continental, marine, mineral dust, and smoke aerosol, Winker et al., 2009). Thus, Polly^{NET} is a valuable tool for satellite validation.

A review of published results of measurements within Polly^{NET} is given in the following. Focus is set on observations in Asia (Sect. 3.1), in the Southern Hemisphere

ACPD
15, 27943–28004, 2015

(Sect. 3.2), on the Atlantic Ocean (Sect. 3.3), and within the European Aerosol Research Lidar Network EARLINET (Sect. 3.4).

3.1 Asia

In October 2004, first Raman lidar measurement with the 1st Polly were performed in Xinken (22.6° N, 113.6° E, 5 m a.s.l.), Pearl River Delta (PRD), China. Haze layers were observed up to 3 km a.g.l. during the diurnal cycle. The particle optical depth (AOD, 532 nm) ranged from 0.3 to 1.7 (average 0.92). The mean lidar ratio of the haze layer was 35 to 59 sr (average 47 sr) (Ansmann et al., 2005; Müller et al., 2006). The observations were continued in Beijing, China in January 2005. In contrast to PRD, almost clean air was observed throughout the Beijing campaign and the observed air masses generally originated from the greater Gobi area (arid desert and steppe). Very low lidar ratios of approximately 25 sr were found in a case of background aerosol conditions with an AOD of 0.05 (Tesche et al., 2007, 2008). For dust- and pollution-loaded air, the extinction coefficients varied between 100 and 300 $M m^{-1}$ and lidar ratios of 30 to 45 sr were observed within the PBL.

In 2009/10, the 1st Polly returned to the area of Beijing. In the framework of the European Aerosol Cloud Climate and Air Quality Interactions (EUCAARI, Kulmala et al., 2011), Polly was operated at the Global Atmospheric Watch station of Shangdianzi (SDZ, 40.6° N, 117° E, 225 m a.s.l.) ca. 100 km north-east of Beijing (Hänel et al., 2012) for one year to cover a full annual cycle. A statistical analysis of all night-time observations showed a distinct haze layer up to 1.5 and a second layer up to 2.5–5 km a.g.l. The extinction coefficient was 200–600 $M m^{-1}$ in the haze layer and 50–100 $M m^{-1}$ in the elevated layer. The column AOD ranged from about 0.3 during northerly air flows to about 0.95 during southerly air flows. The haze layer was characterized with a lidar ratio of about 60 sr indicating anthropogenic fine-mode aerosol. The analysis of the elevated layer showed a broad distribution of the lidar ratio from 40–90 sr caused most probably by a complex mixture of aged desert dust, biomass-burning smoke, and industrial pollution over eastern Asia (Hänel et al., 2012).

ACPD
15, 27943–28004, 2015

The investigation of the vertical aerosol distribution in China was continued in Guangzhou, PRD (23° N, 114° E) from October 2011 for more than half a year in the framework of the project Megacities-Megachallenge funded by the German Research Foundation (DFG). This campaign marked the first deployment of a Polly^{XT} in China. The urban background aerosol of 0.45 AOD showed low particle depolarization ratio of less than 5 %. Lofted layers were observed from 2 to 3.5 km altitude, consisting of a significant fraction of non-spherical dust particles indicated by an increased particle depolarization ratio of 20 % (Heese et al., 2012).

In the framework of EUCAARI, the Finnish Meteorological Institute (FMI) performed measurements with a Polly^{XT} at Gual Pahari (28° N, 77° E, 243 m a.s.l.), close to New Delhi, India for more than one year in 2008 and 2009 (Komppula et al., 2012). Aerosol layers frequently extended up to 5 km altitude. The aerosol characterization showed an annual cycle of continental aerosol during summer (low lidar ratio) and a higher influence of strongly absorbing aerosol in autumn and winter (high lidar ratio). Nevertheless, the mean extinction coefficient between 1 and 3 km a.g.l. was highest during summer (142 M m^{-1} at 532 nm).

The most eastern Polly^{NET} measurement site is at Baengnyeong Island, Korea (38° N, 125° E). The long-term observations started in autumn 2010 and are still ongoing. The PBL usually extends up to 1.2–1.4 km a.g.l. Frequently, lofted layers at altitudes from 2.4–2.8 and 5.2–5.8 km were observed. A high amount of continental aerosol, especially Asian dust, was found with values of the particle depolarization ratio larger than 25 %. The measurements are ongoing and are input for a detailed analysis of Asian dust and pollution, its optical properties, and vertical distribution.

3.2 Southern Hemisphere

A highlight in Polly^{NET} are the first multiwavelength Raman and polarization lidar observations of optical and microphysical particle properties in the Amazon Basin (close to Manaus, Brazil, 3° S, 60° W) from January to November 2008 (Baars et al., 2012) performed in the framework of EUCAARI. The analysis of all measurements

ACPD
15, 27943–28004, 2015

showed strong differences between the pristine wet and the polluted dry season. During the wet season African smoke and dust advection frequently interrupted the pristine phases (Ansmann et al., 2009; Baars et al., 2011). Under pure pristine conditions, the extinction coefficients and AOD (532 nm) were as low as 10–30 $M m^{-1}$ and < 0.05, respectively. In contrast, biomass-burning smoke plumes up to 3–5 km altitude showed extinction coefficients of the order of 100 $M m^{-1}$ and an AOD of 0.26 during the dry season. Ångström exponents were 1.0–1.5, and the observed lidar ratios at 355 and 532 nm were 50–80 sr (Baars et al., 2011, 2012). Seifert et al. (2015) studied the relationship between aerosol properties, temperature, and the efficiency of heterogeneous ice formation in thin stratiform clouds using the data set obtained in Brazil. It was found that the fraction of ice-containing clouds was enhanced by a factor of 1.5 to 2 in the dry compared to the wet season.

Another EUCAARI experiment was performed at Elandsfontein (25° S, 27° E, 2.7 km a.s.l.), South Africa from 2009 to 2011 (Korhonen et al., 2014; Giannakaki et al., 2015). The PBL extended up to 1.4–2.2 km a.g.l. Lofted layers (mean altitude 2.1–2.5 km) were observed throughout the measurement period and showed a high variability in their optical properties and their contribution to the total AOD, due to different source areas and travel paths. Mean lidar ratios at 355 nm were 57 ± 20 sr (December to February), 59 ± 22 sr (March to May), 65 ± 23 sr (June to August), and 89 ± 21 sr (September to November). During southern hemispheric spring a considerable fraction of light-absorbing biomass-burning aerosol was identified in the lofted layers by high lidar ratios.

Shorter measurement campaigns of a few months were performed at Punta Arenas, Chile and Stellenbosch, South Africa (Kanitz et al., 2013a). At the University of the Magellanes, the southernmost multiwavelength Raman and polarization lidar measurements were performed with a Polly^{XT} in 2009/10 for about four month (Kanitz et al., 2014a). Within this period, optically thin lofted layers were observed only eight times during the 24/7 measurements. These layers could be tracked backwards to Australian bush fires and to the Patagonian desert. However, the atmospheric conditions were

ACPD
15, 27943–28004, 2015

dominated by the marine and clean continental background as indicated by AODs lower than 0.05 in about 95 % of all cases (Kanitz et al., 2013a). The PBL extended usually up to 1.2 km a.g.l.

Based on these measurements and the *Polarstern* cruise data, Kanitz et al. (2011) contrasted the temperature dependence of heterogeneous ice formation efficiency between the southern and Northern Hemispheres. At comparable temperatures, a much higher fraction of ice-containing clouds was found in the Northern Hemisphere, suggesting that the increased aerosol load in the northern-hemispheric free troposphere is responsible for this contrast.

3.3 Shipborne measurements

Polly lidar observations have been performed aboard the German research vessel *Polarstern* since 2009. The aerosol data set of the first two years was used to characterize the vertical aerosol distribution over the Atlantic Ocean in both hemispheres. The maximum mean AOD (532 nm) of 0.27 was found in the Saharan outflow region (0–15° N). The mean AOD of the marine background aerosol over the ocean was about 0.05. The AOD was found to be 1.6 times higher at northern midlatitudes (30–60°) compared to their southern counterpart. The extinction coefficient for the vertical column from 1–5 km (lofted aerosol above the marine boundary layer) was 2.5 times higher in the Northern Hemisphere.

Lofted layers of Patagonian dust were observed up to 4 km altitude near the east coast of Argentina. A layer with very low AOD of 0.02–0.03 showed a dust-related lidar ratio of 42 ± 17 sr at 532 nm. At the west coast of North Africa pure Saharan dust (lidar ratio of 50–60 sr at 355 and 532 nm), and mixed dust/smoke plumes (about 60 sr at 355 nm and 45 sr at 532 nm) were observed (Kanitz et al., 2013a).

The second research vessel used as a platform for Polly is the German *Meteor*. A cross section of the Saharan dust layer was recorded during a latitudinal transect from the Caribbean to the west coast of Africa (Cape Verde). The optical properties of aged Saharan dust were determined 4500 km away from the source region with

ACPD
15, 27943–28004, 2015

a transport time of > 10 days and for fresh dust after 2–3 days close to the Saharan desert. The aged dust showed a lidar ratio of about 45 sr and a particle linear depolarization ratio of about 20 % for both wavelengths of 355 and 532 nm. For the fresh dust layer, mean lidar ratios of 64 and 50 sr and particle linear depolarization ratios of 22 and 26 % at 355 and 532 nm wavelength, respectively, were determined (Kanitz et al., 2014b).

3.4 Long-term measurements at four European sites within EARLINET

EARLINET is a scientific network of ground-based aerosol lidars with coordinated measurement times and harmonized data quality assurance (Pappalardo et al., 2014). Polly systems fulfill the EARLINET requirements for instrumental quality assurance and are operated at four of the 28 EARLINET measurement sites (Leipzig, Kuopio and Évora; Warsaw is in the one-year EARLINET validation period).

At TROPOS in Leipzig, Germany, continuous observations with Polly systems have been performed since 2006 and thus the most comprehensive data set within Polly^{NET} is available for this location. Measurements with the first Polly system were used to develop an automated algorithm for PBL-top determination. Maximum PBL-top heights extended up to 1.4, 1.8, 1.2, and 0.8 km in spring, summer, autumn, and winter, respectively (Baars et al., 2008). Analysis of the intensive aerosol properties showed the following aerosol types ordered by the frequency of occurrence: urban/pollution aerosol, Saharan dust and corresponding mixtures, aged biomass-burning aerosol, and volcanic ash. The lidar ratio and depolarization ratio at 355 nm were found to range from 45–65 sr and 0–7 %, respectively, for urban pollution, from 30–60 sr and 7–13 % for dusty mixtures, and from 42–67 sr and 15–23 % for aged biomass-burning aerosol (Illingworth et al., 2015). Further data at the wavelengths of 532 and 1064 nm can be found in the EARLINET data base (The EARLINET publishing group 2000-2010, 2014).

Polly observations have also been performed by the University of Évora, Portugal since 2011. Clear differences in the intensive optical properties were found for layers of Asian and Saharan dust, anthropogenic aerosol from North America and Europe, and

ACPD
15, 27943–28004, 2015

biomass-burning smoke from North America and from the Iberian Peninsula (Preißler et al., 2013b; Pereira et al., 2014). Three out of four lofted layers were observed during spring and summer. The mean layer height varied between 3.8 ± 1.9 and 2.3 ± 0.9 km in summer and winter, respectively. In a statistical analysis evidence for the impact of travel distance on the aerosol optical properties was found. Aerosol layers of same type showed increasing mean Ångström exponents with increasing travel distance (Preißler et al., 2013b). A lofted layer of Saharan dust was observed with an AOD of up to 1.9 in April 2011 (Preißler et al., 2011). Saharan-dust-specific extinction-related Ångström exponents were 0.0 ± 0.2 with mean lidar ratios of 45 ± 8 and 53 ± 7 sr (355, 532 nm), and a mean particle linear depolarization ratio of 28 ± 4 % (at 532 nm) was found. Pereira et al. (2014) studied relatively fresh forest fire smoke observed in lofted aerosol layers. Particle depolarization ratios of about 5 % were found together with lidar ratios above 60 sr at altitudes higher than 3 km a.g.l. The single-scattering albedo was retrieved via inversion and ranged from 0.82 to 0.92 for the six analyzed layers of forest-fire smoke.

Continuous observations are also available at Kuopio, Finland since 2011 (Hirsikko et al., 2014) and Warsaw, Poland since 2013. Profiles of backscatter and extinction coefficients from the regular EARLINET measurement can be found in the EARLINET data base (access via http://actris.eu) and are regularly published (The EARLINET publishing group 2000-2010, 2014).

Table 2 summarizes the determined aerosol-type-related optical properties within Polly^{NET}. Such knowledge is a valuable input for automated aerosol typing (Illingworth et al., 2015), but also for radiative-transfer calculations. All the results presented above are based on time-consuming manual analysis. To overcome this constraint, an automated retrieval for the determination of aerosol optical properties has been developed and is presented in the next section.

ACPD
15, 27943–28004, 2015

4 Automated determination of quantitative aerosol lidar products

Polly systems are designed to operate continuously, i.e., accumulate up to 2880 raw files per day. Naturally, a robust automatic data analysis algorithm is necessary to make use of such an amount of data. Thanks to equal system setup and data format this could be achieved within Polly^{NET}. The processing chain extends from taking the measurement to obtaining aerosol optical profiles and contains the following steps:

- near-real-time transfer of the measurement data to the data server
- pre-processing of the data (e.g., background and range correction)
- cloud and fog screening
- quality assurance
- search for 30 min periods of suitable conditions for the retrieval of aerosol optical profiles
- determination of the reference height range Δz_{ref} following the approach presented by Freudenthaler (2009)

After these steps the optical profiles are calculated using the well-known optical retrieval algorithms similar to the ones used for the EARLINET Single Calculus Chain (SCC, D'Amico et al., 2015). The choice between the preferred Raman method (Ansmann et al., 1992) and the Klett method (Klett, 1981; Fernald, 1984) is based on the signal-to-noise ratio (SNR) in the channels detecting the Raman scattered light (387 and 607 nm). Then, either profiles of the backscatter and extinction coefficient (Raman method) or the backscatter coefficient only (Klett method) can be determined. From the profile of the volume linear depolarization ratio (EARLINET standards, see Freudenthaler et al., 2009) and the backscatter coefficient profile, the particle linear depolarization ratio is calculated. For high quality in the depolarization measurements, a $\Delta 90^{\circ}$ calibration is automatically performed for the TROPOS, FMI, and UW systems

ACPD
15, 27943–28004, 2015

three times a day since 2012 (for system details and overview see Engelmann et al., 2015). Before the implementation of the Δ90° calibration, the calculation of the linear depolarization ratio was also possible, but needed manual calibration and processing. Thus, automatically retrieved depolarization profiles are only available for systems performing the Δ90° calibration. Finally, the vertical aerosol profiles are stored and displayed at http://polly.tropos.de in near-real time without any manual intervention. The complete procedure for the automatic determination of aerosol optical profiles is illustrated in Fig. 3 and explained in more detail in Appendix A.

The online presentation contains also profiles of mid-level and cirrus clouds, which is important not only for quality assurance but also in applications concerning cloud research. To analyze aerosol optical properties only, which is the focus of this paper, a post-processing is applied offline on the retrieved profiles. This is namely a cloud-screening based on the quantitative optical properties to exclude the afore-mentioned mid-level and cirrus clouds. More details are given in Appendix A.

A measurement example with variable and complex aerosol and cloud layering from Leipzig in August 2012 is discussed in the following to show the potential and applicability of the described algorithms.

5 Saharan dust event on 19–20 August 2012, Leipzig, Germany

In this section, an example for the automated Polly^{NET} data analysis is discussed. Figure 4 presents the temporal evolution of the range-corrected signal at 532 nm observed in Leipzig from 19 to 20 August 2012, together with profiles of the backscatter coefficient determined automatically for 30 min time periods. For the sake of visibility only every second profile is shown. At the bottom of Fig. 4, green and blue lines indicate the choice of the retrieval method, i.e., the Raman method or Klett method (with a lidar ratio of 55 sr as a good representative for most aerosol types, Müller et al., 2007), respectively. Time periods without available retrievals are indicated in red. The algorithm uses the Raman method for the night-time observations and automatically switches to

ACPD
15, 27943–28004, 2015

the Klett method when the SNR in the Raman channel is too low during daytime (solar background). In this specific summer case, Klett backscatter profiles were retrieved from about 04:00 to 19:00 UTC.

The day of 19 August 2012 started with no clouds and a clean free troposphere. From about 10:00 UTC a lofted aerosol layer was observed in the free troposphere between 2 and 5 km a.g.l. Backward trajectory and dust model analysis, as well as EARLINET station alerts, suggested that this aerosol layer contained Saharan dust. This was confirmed by the derived aerosol optical properties (see Fig. 5). From 19 to 21 August, more aerosol layers appeared, resulting in a more complex vertical aerosol distribution. In the morning of 20 August, Saharan dust was finally observed from near surface up to 7 km altitude. While the 19 August was completely cloud-free and a pronounced PBL development was observed, on 20 August clouds on top of the PBL (around 1.5 km) and above the major aerosol layer (up to 12.5 km) occurred and can be seen by high backscatter intensity (white coloring) in Fig. 4. The arrival of a frontal precipitation system shortly before midnight led to an opaque sky with fast descending cloud base. The following precipitation (not shown) on 21 August finally ended the observation of the Saharan dust event over Leipzig. Note the change of the intensity in signal due to a change in the neutral-density filter strength on 20 August at around 08:15 UTC.

First, the automatic retrieval focusing on the 532 nm backscatter coefficient on 19 August is discussed. During this day, 42 out of 48 possible 30 min profiles of the backscatter coefficient (532 nm) could be determined and thus an excellent coverage of the aerosol conditions was achieved. The retrieval of the remaining six profiles (between 05:10–05:40, 11:10–11:40, 14:50–15:30, and 16:00–17:00 UTC) failed due to the strict constraints for finding an appropriate reference height (Sect. A5). Most of these cases were rejected due to the increased background noise at higher altitudes during the day so that no automatic reference altitude range could be properly identified. At 355 nm, 44 profiles could be determined (not shown), while at 1064 nm, 41 profiles were derived (not shown). The slightly decreasing number of profiles is due to the

ACPD
15, 27943–28004, 2015

increasing difficulties in calibration at longer wavelengths due to the smaller contribution of molecular scattering to the total scattering.

On 20 August 2012, the complex aerosol layering and the presence of clouds complicated an unambiguous determination of particle backscatter coefficient profiles. However, the automatic analysis performed very well for this day. Neither the neutral-density filter change around 08:15 UTC nor the occasional occurrence of clouds led to disturbed particle backscatter coefficient profiles and in total 23 profiles of the backscatter coefficient at 532 nm could be retrieved (9 and 13 profiles at 355 and 1064 nm, respectively). The low number of profiles is mainly due to the strict constraints concerning reference height retrieval in connection with the decreased SNR during daytime. A considerably good coverage was observed from midnight until noon. Later, occasional clouds above the Saharan dust layer and the high solar elevation angle (low SNR) prohibited an automatic determination of the reference height. With the beginning of the frontal overpass at around 18:00 UTC on 20 August 2012, aerosol profiles could only be retrieved occasionally depending on the presence of low and mid-level clouds during this period.

Note that the threshold values (Appendix A) could be adjusted to retrieve a higher number of profiles. However, the automated algorithm has been strictly designed to produce reliable profiles for many different and complex atmospheric conditions. This leads to a decreased coverage for specific scenarios for which the strict constraints of the retrieval dismiss the determination of a reference height.

During the development of the automated retrieval and the search of best-practice threshold values, the automatically determined profiles have been compared with manually analyzed profiles for specific time periods. For the presented observation from 19 to 20 August 2012, the time period of 19 August 19:00–20:00 UTC was selected to show the evaluation of the automated retrieval. While the manual standard EARLINET analysis was performed for the usual 1 h averaging time, the automated analysis was kept in 30 min averaging mode. Thus, the two closest profiles around that EARLINET analysis time period were used in the comparison effort shown in Fig. 5. Error bars are

ACPD
15, 27943–28004, 2015

not presented for clarity of the illustration but are provided in the data base. Typically, uncertainties are in the range of 5–10 % for the backscatter coefficient and 10–20 % for the extinction coefficient retrieved with the Raman method (Althausen et al., 2009; Baars et al., 2012; Engelmann et al., 2015).

A very good agreement was found for the manually and automatically derived particle backscatter coefficients (Fig. 5, top panel). The backscatter coefficient at 532 nm is nearly identical and only the temporal variation leads to small differences. At 355 nm, the agreement in the Saharan dust layer is good, while there are differences in the PBL (no profiles at 355 nm are available below 500 m because of detector problems at 387 nm). These differences are partly related to high temporal aerosol variability in the PBL, which is more pronounced at shorter wavelengths for small particles. At 1064 nm the agreement is reasonably good considering the well-known difficulties in calibrating the 1064 nm backscatter coefficient (Heese et al., 2010). The profiles of the extinction coefficients, which are determined with the Raman method and thus without the application of a reference height interval, show a very good agreement considering only 30 min averaging of the weak Raman channels (Fig. 5, bottom, left and center). No information is given below 1 km a.g.l. due to the incomplete overlap of the laser beam and the receiver field of view.

The comparison of the volume and particle depolarization ratio (Fig. 5, bottom right) shows a very good agreement and confirms the robustness of the $\Delta 90^{\circ}$ calibration, which was developed within EARLINET during the last years (Pappalardo et al., 2014) and leads to significant improvements for depolarization measurements.

The example above demonstrates that the developed automatic data analysis algorithm works well even under complex atmospheric conditions. The algorithm has been applied on the complete data set of Polly^{NET} until end of 2014 and the results are presented in the following section.

ACPD
15, 27943–28004, 2015

6 Automatically retrieved aerosol profiles from Polly^{NET}

The complete data set of Polly^{NET} was processed with the automatic algorithm described in Sect. 4 and Appendix A. The Polly systems differ in their capabilities and characteristics (Engelmann et al., 2015), e.g., full overlap height, wavelengths detected etc. and thus the derived optical quantities reach from single Raman solutions at 532 nm (like the 1st generation Polly) to 3 + 2 + 1 and 3 + 2 + 2 + 1 + 1 + 1 data for the latest generation of Polly systems. As all Pollys have at least the elastic channel at 532 nm and the corresponding Raman channel at 607 nm, the overview is given in terms of the particle backscatter coefficient at 532 nm to present the most complete set of vertically resolved aerosol optical properties covering day and night observed within Polly^{NET}.

6.1 Overview

An overview of all derived 30 min particle backscatter coefficient profiles at each location is given in Fig. 6. Light grey lines indicate the single profiles and, thus, the variability of the vertical aerosol distribution at each site. In addition, the mean (black), the median (blue), the 25- and 75 %-percentile (purple), and the 5- and 95 %-percentile (red) profiles are plotted.

The top panel of Fig. 6 shows the results for the four measurement locations in Northern Europe: Åre, Stockholm, Hyytiälä, and Kuopio, followed by the Central European stations Cabauw, Krauthausen, Leipzig, and Warsaw. The results of the Southern European stations at Évora and Finokalia and for the shipborne observations aboard *Polarstern* and *Meteor* are given in the center panel. Below, the determined profiles for the Asian sites Delhi, PRD, Beijing, and Baengnyeong are shown. The last panel presents the derived profiles of the particle backscatter coefficient at the stations Punta Arenas, Manaus, Stellenbosch, and Elandsfontein (Southern Hemisphere).

From Fig. 6 one can see the different climatological aerosol conditions at the different locations. The highest aerosol load was determined in China in the height

ACPD
15, 27943–28004, 2015

range below 1 km with values of the 75 % (PRD) and 95 % (Beijing) percentile of 7.8 and 23 $M m^{-1} sr^{-1}$, respectively. In contrast, the aerosol conditions at Punta Arenas can be regarded as pristine, marine conditions with backscatter coefficients less than 1.5 $M m^{-1} sr^{-1}$ in more than 95 % of all observations. The overview of the European sites shows an increase of the vertical extent of free-tropospheric aerosol layers from northern to southern Europe, and also from the western to the eastern sites.

As expected for northern European stations, the observed aerosol load was very low (typically less than 2 $M m^{-1} sr^{-1}$ in the PBL). In Stockholm and Hyytiälä, a slightly stronger particle backscatter was observed on average compared to the other two sites, probably due to the fact that observations were only performed in the summer half year. The main aerosol load was usually trapped in the lowermost 1–2 km at all sites.

Compared to Northern Europe, the vertical aerosol profiles in Central Europe were significantly different. At Cabauw, a coastal but also heavily populated area, almost no aerosol was observed above 3 km. There, most of the aerosol was trapped within the marine-influenced PBL, which did not exceed 1 km in depth during the autumn observations.

As typical for continental sites, a higher aerosol load, a stronger aerosol variability, and a larger vertical extent of aerosol was observed at Krauthausen, Leipzig, and Warsaw compared to the Nordic countries and Cabauw. One has to mention that only for Leipzig a representative long-term statistic is available. On average, aerosol seems to prevail in the lowermost 3 km for all Central European sites, while for Warsaw a slightly higher mean value above 2 km was observed compared to the other locations. Maximum values (95 % percentile profile) increase from West to East (left to right in Fig. 6) and confirms the findings reported in Wandinger et al. (2004).

The profiles recorded at Évora and Finokalia (Fig. 6, center panel) show significant aerosol load up to 5 km. The measurements at these sites were performed in the outflow of the deserts of North Africa. Primarily dust and mixed-dust layers contributed to the high aerosol load in the free troposphere.

ACPD
15, 27943–28004, 2015

The same is valid for the *Meteor* cruise (also Fig. 6, center panel) which was primarily performed to track the Saharan dust layer over the Atlantic Ocean. The north-south cross sections made aboard *Polarstern* were also influenced by dust when the research vessel passed the West African coast. For the shipborne observations, a steep increase in particle backscattering was observed in the transition from the free troposphere to the boundary layer of about 1 km depth. This was most probably caused by marine aerosol that is constantly present over the oceans.

At the Asian sites the vertical aerosol extent was comparably high (up to 5 km a.g.l.). There, anthropogenic aerosol sources contributed significantly to the aerosol load. The Korean site of Baengnyeong has the lowest aerosol load, while in PRD, an economically fast growing region, the strongest mean aerosol backscatter profile was measured. The most extreme values, however, were observed near Beijing (SDZ, 95 %-percentile profile values of 23 $\mathrm{M\,m^{-1}\,sr^{-1}}$). While aerosol was mainly trapped in the lowermost 2 km in PRD (with a weak haze layer up to 3.5 km), at New Delhi, India, aerosol scattering was stronger in the lowest 1 km and was distributed to higher levels with significant aerosol backscatter up to 4 km height. On average, mean values of about 1 $\mathrm{M\,m^{-1}\,sr^{-1}}$ were observed at 3.5 km a.g.l. – more than on average in the PBL at Punta Arenas.

The measurements on the mainlands of the Southern Hemisphere show strong contrasts in the vertical backscatter profiles. At Punta Arenas, in the mid-latitudes of South America, pristine conditions with almost no aerosol in the free troposphere were observed. The aerosol conditions significantly differed near Manaus in Amazonia. Pristine conditions as well as smoke-influenced backscatter profiles were observed. Interestingly, the extreme profiles (95 %-percentile) of high aerosol load are less pronounced than in Leipzig while the vertical extent was similar. Above 5 km, no aerosol was observed at this tropical location during the nearly one-year observation period.

The measurements at the two sites in South Africa, a sub-tropical region, differ significantly from each other. Stellenbosch, which can be regarded as as a coastal site, shows low backscatter coefficients without extreme values throughout the year. Aerosol

ACPD
15, 27943–28004, 2015

was mainly present in the lowermost 3 km. The lidar observations in Elandsfontein took place on a plateau at 1745 m a.s.l. near the urban and industrial area of Johannesburg-Pretoria and were influenced by local smoke and pollution. There, aerosol was observed up to 3.5 km a.g.l., and higher mean and extreme values than in Stellenbosch were observed. Highest values were found close to the ground.

6.2 Seasonal analysis

The Polly^{NET} stations have been partly operated on a continuous long-term basis as in Leipzig, Baengnyeong, Évora, Stockholm, and Kuopio. The most comprehensive dataset exists for Leipzig with 17 749 determined profiles of the backscatter coefficient collected within nine years. Such stations allow for an analysis with respect to different seasons. The seasonal median and extreme profiles may be of particular interest, if representative aerosol profiles at specific locations are needed as a priori input for models or data retrieval algorithms.

Figure 7 shows the automatically determined 532 nm backscatter coefficient profiles for spring (March to May: MAM), summer (June to August: JJA), autumn (September to November: SON), and winter (December to February: DJF) for the five stations mentioned above. The Northern European sites Kuopio and Stockholm show a similar seasonal cycle. Aerosol above the PBL was usually observed in summertime only. Then aerosol was occasionally observed up to the tropopause. These lofted aerosol layers originated usually from wild fires in the sub-Arctic hemisphere, namely Alaska, Canada, and Siberia (e.g., Müller et al., 2005). In wintertime, aerosol was usually trapped in the PBL, which was often below the detection limit of the lidars of 500 m. Domestic heating is the major source of particulate pollution during this part of the year. Spring and autumn were very clean seasons at both locations, with aerosol below 1 km. As during winter, almost no lofted aerosol layers were observed during these seasons.

Leipzig is representative for a moderately polluted, continental, mid-latitude site. While spring and summer show almost no differences above 1.8 km a.g.l., it is obvious that the lowest aerosol load was observed during autumn due to frequent wash

ACPD
15, 27943–28004, 2015

out. In winter, local emissions increased the aerosol load in the lowermost 1.5 km while free-tropospheric aerosol layers were rare. Advection of Saharan dust and long-range-transported smoke occurred typically from spring to early autumn visible by the increased 75 % and 95 %-percentile profile above the PBL of these seasons.

For Évora, representative for southwestern Europe, the median profiles are very similar for all seasons, which reflects a strong marine influence of the Atlantic Ocean. However, the 75 and 95 %-percentile profile clearly show the Saharan dust season in Évora, which was strongest during spring and summer. During this time, aerosol up to 5 km was detected with high particle backscatter coefficients.

At the Korean site of Baengnyeong Island, a pronounced seasonal aerosol structure is visible for all backscatter profiles. Aerosol above the marine PBL (1 km in depth on average) was observed relatively often during the Asian dust season in spring. In summer, frequently lofted aerosol layers up to 4 km height were observed during the rare measurements (N = 15). There were two distinct patterns: aerosol within the PBL and directly above, and a PBL-independent lofted aerosol layer advected between 2 and 4 km. Also evident is the high relative humidity during the summer months in Korea, which is revealed by the increasing backscatter coefficient with height within the PBL (on average below 1.5 km in depth). Aerosol conditions during autumn were similar to those in spring, while in wintertime a shallow PBL and occasional lofted aerosol layers up to 3 km were observed.

7 Conclusions

Thanks to continuous efforts in hardware developments and the resulting instrumental automation, a powerful global network of Raman-polarization lidar systems could be established with Polly^{NET}. Permanent as well as temporary sites form a network of Polly instruments which range from single-wavelength Raman lidars (first version) to two-telescope multiwavelength-Raman-polarization lidars (latest development). A brief review of milestones illustrates the potential of such a network with respect to aerosol

ACPD
15, 27943–28004, 2015

typing and the development of a global aerosol climatology. The lidar data collected within Polly^{NET} between 2006 and 2014 were used as input to an automated data processing procedure which is described in this paper.

For all 21 measurement locations, more than 55 000 30 min backscatter profiles, either determined with the Raman or the Klett method at 532 nm, were retrieved. From that data set, the vertical aerosol distribution and its quantification in terms of particle backscatter for the Northern European, Central European, Southern European, Asian, and Southern Hemispheric sites as well as for the ship cruises across the Atlantic Ocean was discussed. The most extreme values were determined in China in the vertical height range below 1 km with values of the 75 % (PRD) and 95 % (Beijing) percentile of 7.8 and 23 $M m^{-1} sr^{-1}$, respectively. In comparison, the aerosol conditions at Punta Arenas can be regarded as pristine, marine conditions with backscatter coefficients smaller than 1.5 $M m^{-1} sr^{-1}$ in more than 95 % of all observations. The strongest vertical extent of aerosol layers was observed at New Delhi, India, with significant aerosol load up to typically 4 km. The overview of the European sites shows an increase of the vertical extent of free-tropospheric aerosol from northern to southern Europe, and also from the western to the eastern sites. Furthermore, a seasonal analysis has been performed for the long-term sites, which shows the potential of such a global Raman lidar network in supporting the establishment of a global aerosol climatology covering the whole troposphere. All currently analyzed data are shown online at http://polly.tropos.de and are available on demand for further use in agreement with the respective station representatives.

8 Future work

Polly observations with extended near-range capabilities have been used on a prototype basis to perform closure studies with ground-based observations of the Spectral Aerosol Extinction Monitoring System (SAEMS, Skupin et al., 2014) and unmanned airborne vehicles (UAV, Altstädter et al., 2015). In the future, such closure studies will be

ACPD
15, 27943–28004, 2015

done more frequently due to the extension of the atmospheric monitoring site Melpitz, near Leipzig, Germany, to a new European Supersite for aerosol and cloud observations. The upgraded site will include a Polly system, a mobile SAEMS, and the already available ground-based in-situ instrumentation for aerosol characterization. The combination of Polly with cloud radar measurements showed promising results (Bühl et al., 2013) and will be further exploited in future studies.

Polly^{NET} will be expanding over the next years, and Polly systems of the latest standards are planned for new permanent sites at the GAW/ACTRIS site of Finokalia (Crete/Greece), at the GAW observatory of the German Meteorological Service at Hohenpeißenberg, and at the new TROPOS outpost at Mindelo (Cape Verde). Furthermore, temporary observations in Tajikistan, Cyprus, Israel, and the Arctic aboard *Polarstern* are already ongoing or scheduled for the near future. Thanks to the growing 4-D aerosol climatology and the UV capabilities, Polly^{NET} will significantly contribute to the ground-truthing studies in support of the future space-borne lidars onboard ESA's Aeolus and EarthCARE satellites.

Future activities will include the implementation of an automated layer detection algorithm and additional quality-control measures designed to enable the automated estimation of aerosol-type-dependent intensive aerosol properties. These efforts will be done in close collaboration with EARLINET and will lead to a further merging of Polly^{NET} with EARLINET and Cloudnet in the framework of ACTRIS-2.

Appendix A: Ways towards an automated retrieval for multiwavelength-Raman-polarization lidars

In the following, the automatic retrieval of profiles of the backscatter and extinction coefficient as well as the depolarization ratio is explained. The steps listed below have to be considered to retrieve automatically optical products from the lidar measurements:

ACPD
15, 27943–28004, 2015

1. discard inappropriate weather conditions (fog and precipitation)
2. preprocess signals
   - background and range correction
   - cloud screening
   - temporal averaging
3. determine the reference height range Δz_{ref}
   - calculate Rayleigh fits (Freudenthaler, 2009) for several Δz_{ref}
   - assess the determined Δz_{ref}
   - find the optimum Δz_{ref}
4. calculate profiles of particle backscatter coefficient β_{aer} by applying Δz_{ref}
5. calculate profiles of particle extinction coefficient α_{aer} by the Raman method and volume and particle linear depolarization ratio.

An overview of the retrieval steps is given in Fig. A1. The single steps are explained below.

A1 Discard inappropriate weather conditions

During rain events the roof cover of a Polly closes automatically, the laser is switched off, but the data acquisition is ongoing so that the netcdf data file is continuous. Thus, such rain events can be easily monitored. In case of fog, the regular analysis is prohibited due to high atmospheric attenuation of the emitted light within a very low height range. Such measurement periods are identified and flagged, if the raw lidar signal level is lower than 30 photon counts in total within the first 300 to 900 m. The corresponding rain or fog flagged lidar profiles are discarded from further analysis.

ACPD
15, 27943–28004, 2015

A2 Lidar signal preprocessing: raw signal correction

Each acquired raw lidar signal is corrected for background and range. Because in Polly systems only photon counting is applied, no dark-current correction has to be made. Afterward, a overlap correction (Wandinger and Ansmann, 2002) is applied for specific systems to improve the near-range capabilities. Polly overlap characteristics do usually not significantly change because of the fixed optical setup and the temperature stable housing. Nevertheless, in worst case the lowest height bins could be affected due to small temperature changes and are thus discarded.

A3 Lidar signal preprocessing: cloud screening

Cloud screening is performed based on range- and background-corrected signals following Baars et al. (2008). The wavelet covariance transform technique (WCT) detects heights at which strong signal peaks exceed a defined threshold value. The signal increase at the base of low clouds (liquid water) is typically much stronger than at lofted aerosol layers. This allows us to identify low-level clouds in the lidar signal and to flag them in the data quality information. High clouds, especially cirrus, may not be effectively screened, but this is not of interest as long as a reference height range can be found (see Sect. A5). Cirrus can be removed later after the determination of the optical products (see Sect. A6).

The cloud screening is performed with the raw temporal resolution of 30 s. In case of insufficient SNR, e. g., due to very clean air intrusion, the averaging period increases up to 300 s. Below the instrument characteristic minimum overlap height (200 m), i.e., up to this height no overlap between the receiver-field-of-view and the laser beam is achieved, low-level clouds cannot be identified. However, those measurements would have been already flagged as fog (see Sect. A1) and are thus not considered anymore.

The data processing steps for cloud screening are summarized in the following:

1. Calculation of SNR (Heese et al., 2010).

ACPD
15, 27943–28004, 2015

2. Calculation of the normalized WCT (Baars et al., 2008).

3. A cloud base is detected at the height at which the normalized WCT falls first below a threshold of −0.1 (355 nm) or −0.3 (532 and 1064 nm, Baars et al., 2008) above 200 m a.g.l. and with SNR > 2. The SNR threshold is used to avoid mal-detection due to noise.

After the whole measurement period was analyzed and screened for clouds, the preprocessing algorithm looks for as many as possible 30 min intervals that are completely flagged as cloud-free in the lowermost 9 km.

A4 Lidar signal preprocessing: averaging of cloud-free signals

The range- and background-corrected lidar signals in the selected 30 min intervals are averaged and serve as input for the reference height finding procedure. The search for the cloud-free signals is continuous and not fixed to specific times, i.e., the 30 min average interval is moved in raw-resolution steps signal by signal until a clear-sky interval is found. This has the advantage that the occasional short occurrence of low clouds, as often observed at marine locations, does not significantly disturb the analysis of the whole measurement period. The only disadvantage is that the final 30 min backscatter profiles are not in the same time periods for each day. The 30 min averaging is applied to the lidar signals in order to increase the SNR. Lower temporal resolutions are only used, if the analysis focuses on short-term processes during the day, e.g., for specific 2-D radiative transfer calculations.

A5 Automatic reference height determination

In the following, a new approach to find automatically the reference height z_{ref} is presented based on the ideas of Freudenthaler (2009). z_{ref} covers usually an interval of up to 2000 m which is denominated as Δz_{ref}. The selection of a single height bin (7.5–37.5 m) has been avoided considering the influence of noise on the final backscattering

ACPD
15, 27943–28004, 2015

retrieval. For the search of the best suited reference height interval Δz_{ref}, the Rayleigh fit is performed for as many as possible height intervals Δz_{test} of width from 500 to 1000 m, for which the total SNR is greater than the threshold. The threshold value is wavelength dependent and ranges from 1 to 2. Several tests are performed to obtain the quality of all Δz_{test} for being an appropriate Δz_{ref}. Finally, the Δz_{test} with the best quality test results is selected as reference. On the other hand, if no suitable Δz_{ref} can be found, no backscatter profile is retrieved. The detailed approach to derive the reference height range Δz_{ref} for the Polly systems at 355, 532, and 1064 nm is described in the following.

A5.1 Rayleigh fit

For the reference height range Δz_{ref} high altitudes are preferred in order to have aerosol-free conditions at which only Rayleigh scattering at molecules occurs. The Rayleigh scattering in pure molecular air at the height z and the wavelength λ can be easily calculated from profiles of temperature and pressure (Bucholtz, 1995). For the study presented here, vertical profiles of temperature and pressure from the GDAS (Global Data Assimilation System, http://ready.arl.noaa.gov/gdas1.php) are used for that purpose, while for the near-real-time profiles at the website usually standard atmosphere (SA) data is applied until GDAS data is available and data is reprocessed. As a consequence of pure Rayleigh scattering in Δz_{ref}, the range- and background corrected elastic backscatter signal $P(z)z^2$ in this height range should be completely proportional to the molecular attenuated backscatter coefficient. This can be tested by a so-called Rayleigh fit. The Rayleigh fit, i.e., a lidar signal normalized by the attenuated molecular backscatter coefficient (β_{mol}^{att}) for the reference height interval Δz_{ref}, with a lower and upper boundary of $z_{ref(min)}$ and $z_{ref(max)}$, is calculated for a specific

ACPD
15, 27943–28004, 2015

wavelength λ by

$$P^{\mathrm{norm}}(z,\lambda)z^2 = P(z,\lambda)z^2 \frac{\int_{z_{\mathrm{ref(min)}}}^{z_{\mathrm{ref(max)}}} \beta_{\mathrm{mol}}^{\mathrm{attn}}(z',\lambda)\mathrm{d}z'}{\int_{z_{\mathrm{ref(min)}}}^{z_{\mathrm{ref(max)}}} P(z',\lambda)z'^2\mathrm{d}z'}. \quad \text{(A1)}$$

$\beta_{\mathrm{mol}}^{\mathrm{att}}$ is centered at the reference height z_{ref} in dependence of the molecular backscatter and extinction coefficient β_{mol} and α_{mol} according to the general lidar equation for a pure molecular atmosphere:

$$\beta_{\mathrm{mol}}^{\mathrm{att}}(z,z_{\mathrm{ref}},\lambda) = \beta_{\mathrm{mol}}(z,\lambda)\exp\left[-2\int_{z}^{z_{\mathrm{ref}}} \alpha_{\mathrm{mol}}(z',\lambda)\mathrm{d}z\right]. \quad \text{(A2)}$$

For a better understanding, Fig. A2 visualizes profiles of the Rayleigh fit (i.e. P^{norm}) at 355, 532, and 1064 nm with Δz_{ref} between 8 and 10 km altitude. Regions of pure molecular scattering can be identified by the good agreement between the Rayleigh fit and the observed attenuated molecular backscatter coefficient. However, as soon as aerosols contribute to the scattering and absorption in the atmosphere, the two curves deviate significantly from each other (see Fig. A2 below 7 km). This is much more pronounced at 1064 than at 355 nm as Rayleigh scattering is $\propto \lambda^{-4}$. For the analysis of the 1064 nm channel this has to be considered as it causes difficulties in the calibration of the backscatter coefficient in the IR not only for automatic retrievals. After the Rayleigh fit has been calculated for as many reference height intervals Δz_{test} as possible, quality tests are applied to assess their validity.

A5.2 Quality test 1: pure Rayleigh conditions

The test checks, if the particle-caused extinction is lower than the uncertainty of the measurement (Freudenthaler, 2009). The ratio of the normalized signal and the atten-

ACPD
15, 27943–28004, 2015

uated molecular backscatter coefficient is calculated by

$$\frac{P^{\mathrm{norm}}}{\beta_{\mathrm{mol}}^{\mathrm{att}}} \approx \frac{(\beta_{\mathrm{aer}}+\beta_{\mathrm{mol}})\exp\left(-2\int_0^z(\alpha_{\mathrm{aer}}+\alpha_{\mathrm{mol}})\mathrm{d}z\right)}{\beta_{\mathrm{mol}}\exp\left(-2\int_0^z\alpha_{\mathrm{mol}}\mathrm{d}z\right)}$$

$$=\mathrm{BSR}\exp\left(-2\int_0^z(\alpha_{\mathrm{aer}})\mathrm{d}z\right), \quad \text{(A3)}$$

with the backscatter ratio

$$\mathrm{BSR}=\frac{\beta_{\mathrm{aer}}+\beta_{\mathrm{mol}}}{\beta_{\mathrm{mol}}}. \quad \text{(A4)}$$

If Δz_{test} is characterized by pure Rayleigh conditions, BSR becomes unity and Eq. (A3) can be simplified to

$$\ln\frac{P^{\mathrm{norm}}}{\beta_{\mathrm{mol}}^{\mathrm{att}}} \approx -2\int_0^z(\alpha_{\mathrm{aer}})\mathrm{d}z \quad \text{(A5)}$$

and thus

$$\frac{d}{\mathrm{d}z}\left(\ln\frac{P^{\mathrm{norm}}}{\beta_{\mathrm{mol}}^{\mathrm{att}}}\right) \approx -2\alpha_{\mathrm{aer}}. \quad \text{(A6)}$$

Finally, the particle extinction coefficient can be derived by obtaining the deviation in Eq. (A6) with a least-square fit. The smaller α_{aer}, the better the estimation of pure Rayleigh conditions as $\beta_{\mathrm{aer}} \ll \beta_{\mathrm{mol}}$ is assumed. If the uncertainty $\Delta\alpha_{\mathrm{aer}}$ is higher than α_{aer} itself, Δz_{test} is considered to be of pure Rayleigh conditions and confirmed to be a potential Δz_{ref}.

ACPD
15, 27943–28004, 2015

A5.3 Quality test 2: near- and far-range cross criteria

As also discussed by Freudenthaler (2009), if the lidar signal is normalized in a pure molecular atmosphere (Rayleigh conditions), the corresponding normalized signal should be equal or higher than the molecular signal, but not lower, at all heights. If the latter happens, the residual defined as

$$\text{Residual} = P^{\text{norm}}(z)z^2 - \beta^{\text{att}}_{\text{mol}}(z, z_{\text{ref}}), \tag{A7}$$

is negative and the conditions in Δz_{test} have not been aerosol free. In this case, Δz_{test} is inappropriate and discarded. Due to the nature of noise in the lidar signals, technically the test is performed for profile sections of 500 m width. For each of these profile sections the mean of P^{norm} plus its standard deviation must be larger than the mean of $\beta^{\text{att}}_{\text{mol}}$ minus its standard deviation to pass the test. Of course, this criterion is not valid in the height range of incomplete overlap, which has to be excluded from the test. This test has proven to be a powerful tool to detect signal distortions in Δz_{test}.

It can be concluded, the closer $\beta^{\text{att}}_{\text{mol}}(z, z_{\text{ref}})$ and $P^{\text{norm}}(z)z^2$, the better the agreement, the lower the residuals, and the higher the quality of the test interval with respect to pure Rayleigh conditions. For illustration, the corresponding residuals for the examples in Fig. A2 are given in Fig. A3. The residuals are about zero in Δz_{ref} and are positive when deviating significantly from the molecular attenuated backscatter coefficient profile. Thus, for this example the test is successful and Δz_{test} accepted for further testing.

A5.4 Quality test 3: white-noise criterion

Lidar signals are influenced by different noise sources. The normalized real lidar signal will consequently deviate from the ideal no-noise lidar signal within Δz_{test}. For pure Rayleigh conditions the deviation should be limited to white noise. Otherwise, signal distortions or particle contributions cannot be excluded. The normalized lidar signal is

ACPD
15, 27943–28004, 2015

checked for only white noise with the Durbin–Watson test (e.g., Backhaus, 1990):

$$d = \frac{\sum_{n=2}^{N} \left(\Delta_n - \Delta_{n-1}\right)^2}{\sum_{n=1}^{N} \left(\Delta_n\right)^2} \approx 2 \text{ with } \Delta = y - y^* \tag{A8}$$

and

$$y = P^{\text{norm}}(z)z^2 - \beta^{\text{att}}_{\text{mol}}(z, z_{\text{ref}}) = \text{Residual}. \tag{A9}$$

y^* is the linear regression of y. No autocorrelation, i.e., perfect white noise, is given for $d = 2$. For $d = 0$ and $d = 4$ correlation and anticorrelation, respectively, is given. As a good compromise between perfect white noise and a little autocorrelation, which is existent in every data series, the success criterion for this test has been defined to $1 < d < 3$.

A5.5 Quality test 4: SNR check

The last prerequisite is a SNR ≥ 5 over the whole test range Δz_{test} of discrete bin range Δi_{ref} (e.g., 33 bins for 1000 m with 30 m vertical raw resolution):

$$\text{SNR}_{\text{test}} = \frac{\sum_{z_{\text{ref(min)}}}^{z_{\text{ref(max)}}} N - \Delta i_{\text{ref}} N_{\text{b}}}{\sqrt{\sum_{z_{test\text{(min)}}}^{z_{test\text{(max)}}} N + N_{\text{b}}}} \geq 5, \tag{A10}$$

with N the raw photon counts and N_{b} the mean background noise.

ACPD
15, 27943–28004, 2015

A5.6 Selection of optimum reference height

From all successfully tested Δz_{test}, the optimum one has to be selected for being Δz_{ref}. For that purpose, the residuals (Eq. A7) are investigated by means of simple statistical tests and a weighting function X is defined to find the minimum deviation from the ideal Δz_{test}:

$$X(\Delta z_{\text{test}}) = |\mu|\sigma|g|msreA^*, \tag{A11}$$

with the absolute mean value μ, the standard deviation σ, the slope g, the mean square root error *msre* from a linear regression, and the Anderson–Darling test coefficient A^* of the Residual.

The lower $|\mu|$, σ, $|g|$, and *msre*, the better is the desired condition. The Anderson–Darling test checks for normal distribution of the residual values leading to a coefficient A^*. The lower the coefficient A^*, the better is the hypothesis of normal distribution. If a certain value is exceeded, the residual values are not normally distributed (Freudenthaler, 2009). As for the ideal Δz_{test}, X would be 0, the reference height interval Δz_{ref} is finally chosen at that Δz_{test} for which the weighting function becomes minimal. Depending on the SNR in the inelastic channel, either the Raman (Ansmann et al., 1992) or Klett–Fernald method (Fernald, 1984) is applied, and thus either particle backscatter and extinction coefficients or particle backscatter coefficient only are calculated. Afterward, the particle depolarization ratio is calculated from the particle backscatter coefficient profile and from the volume depolarization profile, which is directly obtained from the measurements by applying the $\Delta 90^\circ$ method (Freudenthaler et al., 2009).

A6 Postprocessing for aerosol properties

The postprocessing acts as the final quality check for the retrieved profiles of the particle backscatter and extinction coefficients. This is of importance as one wants to create an aerosol climatology and thus needs to exclude profile fragments that are contaminated by light fog or cirrus clouds. It is worth noting that these profiles have passed all

ACPD
15, 27943–28004, 2015

preprocessing tests and thus are valid. However, they have to be excluded within the presented study of this paper as the focus is on aerosols only. The procedure for that is briefly described in the following:

1. The retrieved profile is excluded from the statistics, if the particle backscatter coefficient (532 nm) is higher than 50 $M\,m^{-1}\,sr^{-1}$ below 300 m altitude which indicates fog.

2. Cirrus and other clouds are identified by applying the WCT (Sects. A3 and Baars et al., 2008) on the profile of the backscatter coefficient (dilation of 240 m). The cloud base is detected at the height at which WCT $< -5 \times 10^{-1}\,M\,m^{-1}\,sr^{-1}$ and as a consequence only the backscatter profile up to 120 m (half dilation) below the cloud base is used for the aerosol climatology to avoid the influence of precipitating ice crystals (see Bühl et al., 2013) in the particle profile below the cloud.

3. In addition, if the Klett method is applied, the profile of the backscatter coefficient is set as invalid in the lowermost range of the incomplete overlap (from 700 to 1500 m depending on the Polly type).

After these steps, the remaining profiles are considered to be valid and used for the creation of the aerosol statistics.

Acknowledgements. First of all, we want to thank the TROPOS workshops and staff members for their permanent effort. The idea of Polly has been always supported by the directors of TROPOS Jost Heintzenberg and Andreas Macke. The authors acknowledge support through the following projects and research programs:

- EUCAARI funded by the European Union (FP6, grant no. 036 833-2)
- ACTRIS under grant agreement no. 262 254 of the European Union Seventh Framework Programme (FP7/2007-2013)
- The China National Basic Research and Development Program (2002CB410801 and 2002CB211605 and 2014CB441201)

– “High Definition Clouds and Precipitation for Climate Prediction - HD(CP)2” (FKZ: 01LK1209C and 01LK1212C) funded by Federal Ministry of Education and Research in Germany (BMBF)
– “Megacities-Megachallenge - Informal Dynamics of Global Change” (SPP 1233) funded by the German Research Foundation (DFG)
– FCT (fundação para a Ciência e a tecnologia) under the grant SFRH/BPD/81132/2011 and in the framework of the project FCOMP-01-0124-FEDER-029212 (PDTC/CEO-MET/4222/2012)
– The Gottfried Wilhelm Leibniz Association (OCEANET project in the framework of PAKT)
– BEYOND (funded under: FP7-REGPOT-2012-2013-1) under grant agreement no. 316 210
– National Science Centre, Poland (NCN) Project SONATA-BIS No. 2012/05/E/ST10/01578
– Foundation of science and technology of Poland (FNITP) Grant No. 519/FNITP/115/2010
– *Polarstern* expeditions AWI_PS75_00, AWI_PS77_00, AWI_PS81_00, AWI_PS83_00
– FAPESP and CNPq

We also thank the LBA Central Office at INPA (The Brazilian National Institute for Amazonian Research) for support. Last but not least, we appreciate the contributions of the individuals that have been involved in supporting, enabling, and maintaining Polly measurements over the last decade.

References

Althausen, D., Engelmann, R., Baars, H., Heese, B., Ansmann, A., Müller, D., and Komppula, M.: Portable Raman Lidar PollyXT for automated profiling of aerosol backscatter, extinction, and depolarization, J. Atmos. Ocean. Tech., 26, 2366–2378, doi:10.1175/2009JTECHA1304.1, 2009. 27948, 27950, 27952, 27963

Althausen, D., Engelmann, R., Baars, H., Heese, B., Kanitz, T., Komppula, M., Giannakaki, E., Pfüller, A., Silva, A. M., Preißler, J., Wagner, F., Rascado, J. L., Pereira, S., Lim, J.-H., Ahn, J. Y., Tesche, M., and Stachlewska, I. S.: PollyNET: a network of multiwavelength polarization Raman lidars, Proc. SPIE, 8894, 88940I–88940I-10, doi:10.1117/12.2028921, 2013. 27948

ACPD
15, 27943–28004, 2015

Altstädter, B., Platis, A., Wehner, B., Scholtz, A., Wildmann, N., Hermann, M., Käthner, R., Baars, H., Bange, J., and Lampert, A.: ALADINA – an unmanned research aircraft for observing vertical and horizontal distributions of ultrafine particles within the atmospheric boundary layer, Atmos. Meas. Tech., 8, 1627–1639, doi:10.5194/amt-8-1627-2015, 2015. 27969

Ansmann, A. and Müller, D.: Lidar and atmospheric aerosol particles, in: Lidar – Range-Resolved Optical Remote Sensing of the Atmosphere, edited by: Weitkamp, C., vol. 102 of Springer Series in Optical Sciences, Springer, Berlin/Heidelberg, 105–141, 2005. 27947, 27951

Ansmann, A., Wandinger, U., Riebesell, M., Weitkamp, C., and Michaelis, W.: Independent measurement of extinction and backscatter profiles in cirrus clouds by using a combined Raman elastic-backscatter lidar, Appl. Optics, 31, 7113–7131, doi:10.1364/AO.31.007113, 1992. 27959, 27979

Ansmann, A., Engelmann, R., Althausen, D., Wandinger, U., Hu, M., Zhang, Y., and He, Q.: High aerosol load over the Pearl River Delta, China, observed with Raman lidar and Sun photometer, Geophys. Res. Lett., 32, L13815, doi:10.1029/2005GL023094, 2005. 27953, 27993

Ansmann, A., Baars, H., Tesche, M., Müller, D., Althausen, D., Engelmann, R., Pauliquevis, T., and Artaxo, P.: Dust and smoke transport from Africa to South America: lidar profiling over Cape Verde and the Amazon rainforest, Geophys. Res. Lett., 36, L11802, doi:10.1029/2009GL037923, 2009. 27955, 27993

Ansmann, A., Seifert, P., Tesche, M., and Wandinger, U.: Profiling of fine and coarse particle mass: case studies of Saharan dust and Eyjafjallajökull/Grimsvötn volcanic plumes, Atmos. Chem. Phys., 12, 9399–9415, doi:10.5194/acp-12-9399-2012, 2012. 27947

Antuña, J. C., Landulfo, E., Clemesha, B., Zaratti, F., Quel, E., Bastidas, A., Estevan, R., and Barja, B.: Lidar community in Latin America: a decade of challenges and successes, in: Reviewed and Revised Papers of the 26th International Laser Radar Conference, 25–29 June 2012 Porto Heli, Peloponnesus, Greece, 25–29, 2012. 27948

Baars, H., Ansmann, A., Engelmann, R., and Althausen, D.: Continuous monitoring of the boundary-layer top with lidar, Atmos. Chem. Phys., 8, 7281–7296, doi:10.5194/acp-8-7281-2008, 2008. 27949, 27957, 27972, 27973, 27980

Baars, H., Ansmann, A., Althausen, D., Engelmann, R., Artaxo, P., Pauliquevis, T., and Souza, R.: Further evidence for significant smoke transport from Africa to Amazonia, Geophys. Res. Lett., 38, L20802, doi:10.1029/2011GL049200, 2011. 27955

ACPD
15, 27943–28004, 2015

Baars, H., Ansmann, A., Althausen, D., Engelmann, R., Heese, B., Müller, D., Artaxo, P., Paixao, M., Pauliquevis, T., and Souza, R.: Aerosol profiling with lidar in the Amazon Basin during the wet and dry season, J. Geophys. Res.-Atmos., 117, D21201, doi:10.1029/2012JD018338, 2012. 27948, 27951, 27954, 27955, 27963, 27993

Backhaus, K.: Multivariate Analysemethoden: Eine anwendungsorientierte Einführung, mit 137 Tabellen, 6th edn., Springer, Berlin, 1990. 27978

Barbosa, H. M. J., Lopes, F. J. S., Silva, A., Nisperuza, D., Barja, B., Ristori, P., Gouveia, D. A., Jimenez, C., Montilla, E., Mariano, G. L., Landulfo, E., Bastidas, A., and Quel, E. J.: The first ALINE measurements and intercomparison exercise on lidar inversion algorithms, Optica pura y aplicada, 47, 99–108, doi:10.7149/OPA.47.2.109, 2014. 27948

Binietoglou, I., Basart, S., Alados-Arboledas, L., Amiridis, V., Argyrouli, A., Baars, H., Baldasano, J. M., Balis, D., Belegante, L., Bravo-Aranda, J. A., Burlizzi, P., Carrasco, V., Chaikovsky, A., Comerón, A., D'Amico, G., Filioglou, M., Granados-Muñoz, M. J., Guerrero-Rascado, J. L., Ilic, L., Kokkalis, P., Maurizi, A., Mona, L., Monti, F., Muñoz-Porcar, C., Nicolae, D., Papayannis, A., Pappalardo, G., Pejanovic, G., Pereira, S. N., Perrone, M. R., Pietruczuk, A., Posyniak, M., Rocadenbosch, F., Rodríguez-Gómez, A., Sicard, M., Siomos, N., Szkop, A., Terradellas, E., Tsekeri, A., Vukovic, A., Wandinger, U., and Wagner, J.: A methodology for investigating dust model performance using synergistic EARLINET/AERONET dust concentration retrievals, Atmos. Meas. Tech. Discuss., 8, 3605–3666, doi:10.5194/amtd-8-3605-2015, 2015. 27950

Bösenberg, J., Hoff, R., Ansmann, A., Müller, D., Antuña, J., Whiteman, D., Sugimoto, N., Apituley, A., Hardesty, M., Welton, J., Eloranta, E., Arshinov, Y., Kinne, S., and Freudenthaler, V.: Plan for the Implementation of the GAW Aerosol Lidar Observation Network (GALION), WMO/TD, 178, 2007. 27947

Bucholtz, A.: Rayleigh-scattering calculations for the terrestrial atmosphere, Appl. Optics, 34, 2765–2773, 1995. 27974

Bühl, J., Ansmann, A., Seifert, P., Baars, H., and Engelmann, R.: Toward a quantitative characterization of heterogeneous ice formation with lidar/radar: comparison of CALIPSO/CloudSat with ground-based observations, Geophys. Res. Lett., 40, 4404–4408, doi:10.1002/grl.50792, 2013. 27970, 27980

Chaikovsky, A., Ivanov, A., Balin, Y., Elnikov, A., Tulinov, G., Plusnin, I., Bukin, O., and Chen, B.: Lidar network CIS-LiNet for monitoring aerosol and ozone in CIS regions, in: Twelfth Joint International Symposium on Atmospheric and Ocean Optics/Atmospheric Physics, Interna-

ACPD
15, 27943–28004, 2015

tional Society for Optics and Photonics, Proc. SPIE 6160, 616035, doi:10.1117/12.675920, 2006. 27948

D'Amico, G., Amodeo, A., Baars, H., Binietoglou, I., Freudenthaler, V., Mattis, I., Wandinger, U., and Pappalardo, G.: EARLINET Single Calculus Chain – general presentation methodology and strategy, Atmos. Meas. Tech. Discuss., 8, 4973–5023, doi:10.5194/amtd-8-4973-2015, 2015. 27949, 27959

Engelmann, R., Kanitz, T., Baars, H., Heese, B., Althausen, D., Skupin, A., Wandinger, U., Komppula, M., Stachlewska, I. S., Amiridis, V., Marinou, E., Mattis, I., Linné, H., and Ansmann, A.: EARLINET Raman Lidar Polly^{XT}: the neXT generation, Atmos. Meas. Tech. Discuss., 8, 7737–7780, doi:10.5194/amtd-8-7737-2015, 2015. 27948, 27952, 27960, 27963, 27964, 27992

Fernald, F. G.: Analysis of atmospheric lidar observations – some comments, Appl. Optics, 23, 652–653, 1984. 27959, 27979

Flentje, H., Heese, B., Reichardt, J., and Thomas, W.: Aerosol profiling using the ceilometer network of the German Meteorological Service, Atmos. Meas. Tech. Discuss., 3, 3643–3673, doi:10.5194/amtd-3-3643-2010, 2010. 27947

Foth, A., Baars, H., Di Girolamo, P., and Pospichal, B.: Water vapour profiles from Raman lidar automatically calibrated by microwave radiometer data during HOPE, Atmos. Chem. Phys., 15, 7753–7763, doi:10.5194/acp-15-7753-2015, 2015. 27951

Freudenthaler, V.: Lidar Rayleigh-fit criteria, in: EARLINET-ASOS 7th Workshop, available at: http://nbn-resolving.de/urn/resolver.pl?urn=nbn:de:bvb:19-epub-12970-6 (last access: 11 February 2015), 2009. 27959, 27971, 27973, 27975, 27977, 27979

Freudenthaler, V., Esselborn, M., Wiegner, M., Heese, B., Tesche, M., Ansmann, A., Müller, D., Althausen, D., Wirth, M., Fix, A., Ehret, G., Knippertz, P., Toledano, C., Gasteiger, J., Garhammer, M., and Seefeldner, M.: Depolarization ratio profiling at several wavelengths in pure Saharan dust during SAMUM 2006, Tellus B, 61, 165–179, doi:10.1111/j.1600-0889.2008.00396.x, 2009. 27951, 27959, 27979

Giannakaki, E., Pfüller, A., Korhonen, K., Mielonen, T., Laakso, L., Vakkari, V., Baars, H., Engelmann, R., Beukes, J. P., Van Zyl, P. G., Josipovic, M., Tiitta, P., Chiloane, K., Piketh, S., Lihavainen, H., Lehtinen, K. E. J., and Komppula, M.: One year of Raman lidar observations of free-tropospheric aerosol layers over South Africa, Atmos. Chem. Phys., 15, 5429–5442, doi:10.5194/acp-15-5429-2015, 2015. 27955, 27993, 27994

ACPD
15, 27943–28004, 2015

Hänel, A., Baars, H., Althausen, D., Ansmann, A., Engelmann, R., and Sun, J. Y.: One-year aerosol profiling with EUCAARI Raman lidar at Shangdianzi GAW station: Beijing plume and seasonal variations, J. Geophys. Res.-Atmos, 117, D13201, doi:10.1029/2012JD017577, 2012. 27953, 27993, 27994

Haustein, K., Pérez, C., Baldasano, J. M., Müller, D., Tesche, M., Schladitz, A., Esselborn, M., Weinzierl, B., Kandler, K., and von Hoyningen-Huene, W.: Regional dust model performance during SAMUM 2006, Geophys. Res. Lett., 36, L03812, doi:10.1029/2008GL036463, 2009. 27950

Heese, B., Flentje, H., Althausen, D., Ansmann, A., and Frey, S.: Ceilometer lidar comparison: backscatter coefficient retrieval and signal-to-noise ratio determination, Atmos. Meas. Tech., 3, 1763–1770, doi:10.5194/amt-3-1763-2010, 2010. 27947, 27963, 27972

Heese, B., Althausen, D., Bauditz, M., Bao, R., Deng, R., and Li, Z.: Lidar depolarization and sun photometer polarization measurements for particle characterization over Guangzhou, China, in: Reviewed and Revised Papers of the 26th International Laser Radar Conference, 25–29 June 2012 Porto Heli, Peloponnesus, Greece, 505–509, 2012. 27954

Heese, B., Althausen, D., Baars, H., Bohlmann, S., and Deng, R.: Aerosol properties over Southeastern China from multiwavelength Raman and depolarization lidar measurents, in: Reviewed and Revised Papers of 27th ILRC International Laser Radar Conference 5–10 July 2015, New York, USA, 2015. 27993

Hirsikko, A., O'Connor, E. J., Komppula, M., Korhonen, K., Pfüller, A., Giannakaki, E., Wood, C. R., Bauer-Pfundstein, M., Poikonen, A., Karppinen, T., Lonka, H., Kurri, M., Heinonen, J., Moisseev, D., Asmi, E., Aaltonen, V., Nordbo, A., Rodriguez, E., Lihavainen, H., Laaksonen, A., Lehtinen, K. E. J., Laurila, T., Petäjä, T., Kulmala, M., and Viisanen, Y.: Observing wind, aerosol particles, cloud and precipitation: Finland's new ground-based remote-sensing network, Atmos. Meas. Tech., 7, 1351–1375, doi:10.5194/amt-7-1351-2014, 2014. 27948, 27958

Hoff, R. M. and Pappalardo, G.: The GAW Aerosol Lidar Observation Network (GALION) as a source of near-real time aerosol profile data for model evaluation and assimilation, AGU Fall Meeting Abstracts, p. G8, 2010. 27947

Holben, B. N., Tanré, D., Smirnov, A., Eck, T. F., Slutsker, I., Abuhassan, N., Newcomb, W. W., Schafer, J. S., Chatenet, B., Lavenu, F., Kaufman, Y. J., Castle, J. V., Setzer, A., Markham, B., Clark, D., Frouin, R., Halthore, R., Karneli, A., O'Neill, N. T., Pietras, C., Pinker, R. T., Voss, K.,

ACPD
15, 27943–28004, 2015

and Zibordi, G.: An emerging ground-based aerosol climatology: aerosol optical depth from AERONET, J. Geophys. Res., 106, 12067–12098, doi:10.1029/2001JD900014, 2001. 27948
Illingworth, A. J., Barker, H. W., Beljaars, A., Ceccaldi, M., Chepfer, H., Clerbaux, N., Cole, J., Delanoë, J., Domenech, C., Donovan, D. P., Fukuda, S., Hirakata, M., Hogan, R. J., Huenerbein, A., Kollias, P., Kubota, T., Nakajima, T., Nakajima, T. Y., Nishizawa, T., Ohno, Y., Okamoto, H., Oki, R., Sato, K., Satoh, M., Shephard, M. W., Velázquez-Blázquez, A., Wandinger, U., Wehr, T., and van Zadelhoff, G.-J.: The EarthCARE Satellite: The Next Step Forward in Global Measurements of Clouds, Aerosols, Precipitation, and Radiation, B. Am. Meteorol. Soc., 96, 1311–1332, doi:10.1175/BAMS-D-12-00227.1, 2015. 27950, 27957, 27958, 27993
IPCC: Climate Change 2013: The Physical Science Basis, Contribution of Working Group I to the Fifth Assessment Report of the Intergovernmental Panel on Climate Change, Cambridge University Press, Cambridge, UK, New York, USA, doi:10.1017/CBO9781107415324, available at: http://ebooks.cambridge.org/ebook.jsf?bid=CBO9781107415324 (last access: 8 October 2015), 2014. 27946
Janicka, L., Stachlewska, I., Markowicz, K., Baars, H., Engelmann, R., and Heese, B.: Lidar measurements of Canadian forest fire smoke episode observed in July 2013 over Warsaw, Poland, in: Reviewed and Revised Papers of 27th ILRC International Laser Radar Conference 5–10 July 2015, New York, USA, 2015. 27993
Kanitz, T.: Vertical Distribution of Aerosols Above the Atlantic Ocean, Punta Arenas (Chile), and Stellenbosch (South Africa): Characterization, Solar Radiative Effects and Ice Nucleating Properties, PhD thesis, Technische Universität Berlin, Faculty III Process Sciences, 2012. 27993
Kanitz, T., Seifert, P., Ansmann, A., Engelmann, R., Althausen, D., Casiccia, C., and Rohwer, E. G.: Contrasting the impact of aerosols at northern and southern midlatitudes on heterogeneous ice formation, Geophys. Res. Lett., 38, L17802, doi:10.1029/2011GL048532, 2011. 27956
Kanitz, T., Ansmann, A., Engelmann, R., and Althausen, D.: North-south cross sections of the vertical aerosol distribution over the Atlantic Ocean from multiwavelength Raman/polarization lidar during *Polarstern* cruises, J. Geophys. Res.-Atmos., 118, 2643–2655, doi:10.1002/jgrd.50273, 2013a. 27948, 27951, 27952, 27955, 27956, 27993
Kanitz, T., Ansmann, A., Seifert, P., Engelmann, R., Kalisch, J., and Althausen, D.: Radiative effect of aerosols above the northern and southern Atlantic Ocean as deter-

ACPD
15, 27943–28004, 2015

mined from shipborne lidar observations, J. Geophys. Res.-Atmos., 118, 12556–12565, doi:10.1002/2013JD019750, 2013b. 27950

Kanitz, T., Ansmann, A., Foth, A., Seifert, P., Wandinger, U., Engelmann, R., Baars, H., Althausen, D., Casiccia, C., and Zamorano, F.: Surface matters: limitations of CALIPSO V3 aerosol typing in coastal regions, Atmos. Meas. Tech., 7, 2061–2072, doi:10.5194/amt-7-2061-2014, 2014a. 27955

Kanitz, T., Engelmann, R., Heinold, B., Baars, H., Skupin, A., and Ansmann, A.: Tracking the Saharan Air Layer with shipborne lidar across the tropical Atlantic, Geophys. Res. Lett., 41, 1044–1050, doi:10.1002/2013GL058780, 2014b. 27952, 27957, 27993

Klett, J.: Stable analytical inversion solution for processing lidar returns, Appl. Optics, 20, 211–220, 1981. 27959

Komppula, M., Mielonen, T., Arola, A., Korhonen, K., Lihavainen, H., Hyvärinen, A.-P., Baars, H., Engelmann, R., Althausen, D., Ansmann, A., Müller, D., Panwar, T. S., Hooda, R. K., Sharma, V. P., Kerminen, V.-M., Lehtinen, K. E. J., and Viisanen, Y.: Technical Note: One year of Raman-lidar measurements in Gual Pahari EUCAARI site close to New Delhi in India – Seasonal characteristics of the aerosol vertical structure, Atmos. Chem. Phys., 12, 4513–4524, doi:10.5194/acp-12-4513-2012, 2012. 27954, 27993, 27994

Korhonen, K., Giannakaki, E., Mielonen, T., Pfüller, A., Laakso, L., Vakkari, V., Baars, H., Engelmann, R., Beukes, J. P., Van Zyl, P. G., Ramandh, A., Ntsangwane, L., Josipovic, M., Tiitta, P., Fourie, G., Ngwana, I., Chiloane, K., and Komppula, M.: Atmospheric boundary layer top height in South Africa: measurements with lidar and radiosonde compared to three atmospheric models, Atmos. Chem. Phys., 14, 4263–4278, doi:10.5194/acp-14-4263-2014, 2014. 27955

Kulmala, M., Asmi, A., Lappalainen, H. K., Baltensperger, U., Brenguier, J.-L., Facchini, M. C., Hansson, H.-C., Hov, Ø., O'Dowd, C. D., Pöschl, U., Wiedensohler, A., Boers, R., Boucher, O., de Leeuw, G., Denier van der Gon, H. A. C., Feichter, J., Krejci, R., Laj, P., Lihavainen, H., Lohmann, U., McFiggans, G., Mentel, T., Pilinis, C., Riipinen, I., Schulz, M., Stohl, A., Swietlicki, E., Vignati, E., Alves, C., Amann, M., Ammann, M., Arabas, S., Artaxo, P., Baars, H., Beddows, D. C. S., Bergström, R., Beukes, J. P., Bilde, M., Burkhart, J. F., Canonaco, F., Clegg, S. L., Coe, H., Crumeyrolle, S., D'Anna, B., Decesari, S., Gilardoni, S., Fischer, M., Fjaeraa, A. M., Fountoukis, C., George, C., Gomes, L., Halloran, P., Hamburger, T., Harrison, R. M., Herrmann, H., Hoffmann, T., Hoose, C., Hu, M., Hyvärinen, A., Hõrrak, U., Iinuma, Y., Iversen, T., Josipovic, M., Kanakidou, M., Kiendler-Scharr, A., Kirkevåg, A.,

ACPD
15, 27943–28004, 2015

Kiss, G., Klimont, Z., Kolmonen, P., Komppula, M., Kristjánsson, J.-E., Laakso, L., Laaksonen, A., Labonnote, L., Lanz, V. A., Lehtinen, K. E. J., Rizzo, L. V., Makkonen, R., Manninen, H. E., McMeeking, G., Merikanto, J., Minikin, A., Mirme, S., Morgan, W. T., Nemitz, E., O'Donnell, D., Panwar, T. S., Pawlowska, H., Petzold, A., Pienaar, J. J., Pio, C., Plass-Duelmer, C., Prévôt, A. S. H., Pryor, S., Reddington, C. L., Roberts, G., Rosenfeld, D., Schwarz, J., Seland, Ø., Sellegri, K., Shen, X. J., Shiraiwa, M., Siebert, H., Sierau, B., Simpson, D., Sun, J. Y., Topping, D., Tunved, P., Vaattovaara, P., Vakkari, V., Veefkind, J. P., Visschedijk, A., Vuollekoski, H., Vuolo, R., Wehner, B., Wildt, J., Woodward, S., Worsnop, D. R., van Zadelhoff, G.-J., Zardini, A. A., Zhang, K., van Zyl, P. G., Kerminen, V.-M., S Carslaw, K., and Pandis, S. N.: General overview: European Integrated project on Aerosol Cloud Climate and Air Quality interactions (EUCAARI) – integrating aerosol research from nano to global scales, Atmos. Chem. Phys., 11, 13061–13143, doi:10.5194/acp-11-13061-2011, 2011. 27953

Müller, D., Mattis, I., Wandinger, U., Ansmann, A., Althausen, D., and Stohl, A.: Raman lidar observations of aged Siberian and Canadian forest fire smoke in the free troposphere over Germany in 2003: microphysical particle characterization, J. Geophys. Res., 110, D17201, doi:10.1029/2004JD005756, 2005. 27967

Müller, D., Tesche, M., Eichler, H., Engelmann, R., Althausen, D., Ansmann, A., Cheng, Y. F., Zhang, Y. H., and Hu, M.: Strong particle light absorption over the Pearl River Delta (south China) and Beijing (north China) determined from combined Raman lidar and Sun photometer observations, Geophys. Res. Lett., 33, L20811, doi:10.1029/2006GL027196, 2006. 27953

Müller, D., Ansmann, A., Mattis, I., Tesche, M., Wandinger, U., Althausen, D., and Pisani, G.: Aerosol-type-dependent lidar ratios observed with Raman lidar, J. Geophys. Res., 112, D16202, doi:10.1029/2006JD008292, 2007. 27947, 27951, 27960

Pappalardo, G., Amodeo, A., Apituley, A., Comeron, A., Freudenthaler, V., Linné, H., Ansmann, A., Bösenberg, J., D'Amico, G., Mattis, I., Mona, L., Wandinger, U., Amiridis, V., Alados-Arboledas, L., Nicolae, D., and Wiegner, M.: EARLINET: towards an advanced sustainable European aerosol lidar network, Atmos. Meas. Tech., 7, 2389–2409, doi:10.5194/amt-7-2389-2014, 2014. 27947, 27957, 27963

Pereira, S. N., Preißler, J., Guerrero-Rascado, J. L., Silva, A. M., and Wagner, F.: Forest fire smoke layers observed in the free troposphere over Portugal with a multiwavelength ra-

ACPD
15, 27943–28004, 2015

man lidar: optical and microphysical properties, The Scientific World Journal, 2014, 11 pp., doi:10.1155/2014/421838, 2014. 27958, 27993

Preißler, J., Wagner, F., Pereira, S. N., and Guerrero-Rascado, J. L.: Multi-instrumental observation of an exceptionally strong Saharan dust outbreak over Portugal, J. Geophys. Res.-Atmos., 116, D24204, doi:10.1029/2011JD016527, 2011. 27958, 27993

Preißler, J., Bravo-Aranda, J., Wagner, F., Granados-Muñoz, M. J., Navas-Guzmán, F., Guerrero-Rascado, J. L., Lyamani, H., and Alados-Arboledas, L.: Optical properties of free tropospheric aerosol from multi-wavelength Raman lidars over the southern Iberian Peninsula, in: Proceedings of the 9th International Symposium on Tropospheric Profiling, l'Aquila, Italy, 3–7 September 2012, 2012. 27993

Preißler, J., Pereira, S., Silva, A. M., and Wagner, F.: Vertically resolved optical and microphysical properties of Portuguese forest fire smoke observed in February 2012, Lidar Technologies, Techniques, and Measurements for Atmospheric Remote Sensing IX, Proc. SPIE 8894, 88940Y, doi:10.1117/12.2029184, 2013a. 27993

Preißler, J., Wagner, F., Guerrero-Rascado, J. L., and Silva, A. M.: Two years of free-tropospheric aerosol layers observed over Portugal by lidar, J. Geophys. Res.-Atmos., 118, 3676–3686, doi:10.1002/jgrd.50350, 2013b. 27958, 27993

Reichardt, J., Wandinger, U., Klein, V., Mattis, I., Hilber, B., and Begbie, R.: RAMSES: German Meteorological Service autonomous Raman lidar for water vapor, temperature, aerosol, and cloud measurements, Appl. Optics, 51, 8111–8131, doi:10.1364/AO.51.008111, 2012. 27951

Seifert, P., Kunz, C., Baars, H., Ansmann, A., Bühl, J., Senf, F., Engelmann, R., Althausen, D., and Artaxo, P.: Seasonal variability of heterogeneous ice formation in stratiform clouds over the Amazon Basin, Geophys. Res. Lett., 42, 5587–5593, doi:10.1002/2015GL064068, 2015. 27955

Sicard, M., Guerrero-Rascado, J. L., Navas-Guzmán, F., Preißler, J., Molero, F., Tomás, S., Bravo-Aranda, J. A., Comerón, A., Rocadenbosch, F., Wagner, F., Pujadas, M., and Alados-Arboledas, L.: Monitoring of the Eyjafjallajökull volcanic aerosol plume over the Iberian Peninsula by means of four EARLINET lidar stations, Atmos. Chem. Phys., 12, 3115–3130, doi:10.5194/acp-12-3115-2012, 2012. 27993

Skupin, A., Ansmann, A., Engelmann, R., Baars, H., and Müller, T.: The Spectral Aerosol Extinction Monitoring System (SÆMS): setup, observational products, and comparisons, Atmos. Meas. Tech., 7, 701–712, doi:10.5194/amt-7-701-2014, 2014. 27969

ACPD
15, 27943–28004, 2015

Spinhirne, J. D., Rall, J. A., and Scott, V. S.: Compact eye safe lidar systems, The Review of Laser Engineering, 23, 112–118, doi:10.2184/lsj.23.112, 1995. 27947

Stachlewska, I., Piądłowski, M., Migacz, S., Szkop, A., Zielińska, A., and Swaczyna, P.: Ceilometer observations of the boundary layer over Warsaw, Poland, Acta Geophys., 60, 1386–1412, doi:10.2478/s11600-012-0054-4, 2012. 27947

Stevens, B. and Feingold, G.: Untangling aerosol effects on clouds and precipitation in a buffered system, Nature, 461, 607–613, 2009. 27946

Stoffelen, A., Pailleux, J., Källén, E., Vaughan, J. M., Isaksen, L., Flamant, P., Wergen, W., Andersson, E., Schyberg, H., Culoma, A., Meynart, R., Endemann, M., and Ingmann, P.: The Atmospheric Dynamics Mission for global wind field measurement, B. Am. Meteorol. Soc., 86, 73–87, 2005. 27950

Sugimoto, N., Matsui, I., Shimizu, A., Nishizawa, T., Hara, Y., Xie, C., Uno, I., Yumimoto, K., Wang, Z., and Yoon, S.-C.: Lidar network observations of tropospheric aerosols, Lidar Remote Sensing for Environmental Monitoring IX, Proc. SPIE 7153, 71530A, doi:10.1117/12.806540, 2008. 27948

Sugimoto, N., Nishizawa, T., Shimizu, A., Matsui, I., and Jin, Y.: Characterization of aerosols in East Asia with the Asian Dust and Aerosol Lidar Observation Network (AD-Net), Lidar Remote Sensing for Environmental Monitoring XIV, Proc. SPIE 9262, 92620K, doi:10.1117/12.2069892, 2014. 27948

Tesche, M., Ansmann, A., Müller, D., Althausen, D., Engelmann, R., Hu, M., and Zhang, Y.: Particle backscatter, extinction, and lidar ratio profiling with Raman lidar in south and north China, Appl. Optics, 46, 6302–6308, doi:10.1364/AO.46.006302, 2007. 27953, 27993

Tesche, M., Müller, D., Ansmann, A., Hu, M., and Zhang, Y.: Retrieval of microphysical properties of aerosol particles from one-wavelength Raman lidar and multiwavelength Sun photometer observations, Atmos. Environ., 42, 6398–6404, doi:10.1016/j.atmosenv.2008.02.014, 2008. 27953

Tesche, M., Gross, S., Ansmann, A., Müller, D., Althausen, D., Freudenthaler, V., and Esselborn, M.: Profiling of Saharan dust and biomass-burning smoke with multiwavelength polarization Raman lidar at Cape Verde, Tellus B, 63, 4, doi:10.3402/tellusb.v63i4.16360, 2011. 27951

The EARLINET publishing group 2000–2010: EARLINET All Observations (2000–2010), doi:10.1594/WDCC/EN_all_measurements_2000-2010, 2014. 27957, 27958

ACPD
15, 27943–28004, 2015

Wandinger, U. and Ansmann, A.: Experimental determination of the lidar overlap profile with Raman lidar, Appl. Optics, 41, 511–514, 2002. 27951, 27972

Wandinger, U., Mattis, I., Tesche, M., Ansmann, A., Bösenberg, J., Chaikovski, A., Freudenthaler, V., Komguem, L., Linné, H., Matthias, V., Pelon, J., Sauvage, L., Sobolewski, P., Vaughan, G., and Wiegner, M.: Air mass modification over Europe: EARLINET aerosol observations from Wales to Belarus, J. Geophys. Res.-Atmos., 109, D24205, doi:10.1029/2004JD005142, 2004. 27965

Welton, E. J., Campbell, J. R., Spinhirne, J. D., and Scott III, V. S.: Global monitoring of clouds and aerosols using a network of micropulse lidar systems, in: Second International Asia-Pacific Symposium on Remote Sensing of the Atmosphere, Environment, and Space, International Society for Optics and Photonics, 151–158, doi:10.1117/12.417040, 2001. 27947

Winker, D. M., Vaughan, M. A., Omar, A., Hu, Y., Powell, K. A., Liu, Z., Hunt, W. H., and Young, S. A.: Overview of the CALIPSO mission and CALIOP data processing algorithms, J. Atmos. Ocean. Tech., 26, 2310–2323, 2009. 27947, 27952

ACPD
15, 27943–28004, 2015

Table 1. Overview of measurement sites with location, Polly lidar type (1st – first Polly system owned by TROPOS, OCEANET – Polly^{XT} for shipborne observations owned by TROPOS, all others are Polly^{XT} systems owned by the institution as named, more details see Engelmann et al., 2015), number of available measurement days (status: 31 December 2014 for ongoing measurements), dominant aerosol types, and time period of observation. Considered aerosol types are: clean continental (cc), polluted continental (pc), marine (m), mineral dust (md), and smoke (s).

Site	Latitude	Longitude	Altitude	Used lidar	# days	Aerosol types	Period
Åre, Sweden	63.4° N	13.1° E	425 m	1st	64	cc	Jun 2014–Sep 2014
Athens, Greece	38° N	23.9° E	488 m	NOA		pc, m, md, s	May 2015–ongoing
Baengnyeong, Korea	38° N	124.7° E	20 m	NIER	304	pc, m, md	Oct 2010–ongoing
Beijing, urban, China	39.9° N	116.3° E	60 m	1st	10	cc, pc, md	Jan 2005–Jan 2005
Beijing, rural at SDZ, China	40.7° N	117.1° E	116 m	1st	260	cc, pc, md	Apr 2009–Mar 2010
Cabauw, the Netherlands	52.0° N	4.9° E	−1 m	TROPOS	50	cc, pc, m	Sep 2014–Nov 2014
Dushanbe, Tajikistan	38.6° N	68.9° E	810 m	TROPOS		md, pc, cc	Mar 2015–ongoing
Elandsfontein, South Africa	26.3° S	29.4° E	1745 m	FMI	302	cc, pc, s	Dec 2009–Jan 2011
Évora, Portugal	38.5° N	7.9° W	290 m	UE-ICT	649	cc, m, md, s	May 2009–ongoing
Finokalia, Greece	35.3° N	25.7° E	245 m	OCEANET	35	cc, md, m	Jun 2014–Jul 2014
Hyytiälä, Finland	61.8° N	24.3° E	147 m	FMI	156	cc	Apr 2014–Sep 2014
Krauthausen, Germany	50.9° N	6.4° E	95 m	TROPOS	61	cc, pc	Apr 2013–May 2013
Kuopio, Finland	62.7° N	27.5° E	195 m	FMI	515	cc	Oct 2012–ongoing
Leipzig, Germany	51.4° N	12.4° E	125 m	1st			
				TROPOS			
				OCEANET	1641	cc, pc, md	Jan 2006–ongoing
Lindenberg, Germany	52.2° N	14.1° E	115 m	DWD		cc, pc, md	Jun 2015–ongoing
Manaus, Brazil	2.6° S	60.0° W	83 m	TROPOS	213	cc, s, md	Jan 2008–Nov 2008
Melpitz, Germany	51.5° N	12.9° E	83 m	1st	42	cc, pc, md	May 2008–Jul 2008
				OCEANET	48	cc, pc, md	Sep 2013–Oct 2013
New Delhi (Gual Pahari), India	28.4° N	77.2° E	243 m	FMI	142	pc, s	Mar 2008–Mar 2009
Nicosia, Cyprus	35.1° N	33.4° E	174 m	NOA	43	md, m, s, pc	Mar 2015–Apr 2015
PRD, Xinken, China	22.6° N	113.6° E	10 m	1st	22	pc	Oct 2004–Oct 2004
PRD, Guangzhou, China	23.1° N	113.4° E	25 m	TROPOS	209	pc	Nov 2011–Jun 2012
Punta Arenas, Chile	53.2° S	70.9° W	40 m	TROPOS	96	cc, m	Nov 2009–Mar 2010
Stellenbosch, South Africa	34° S	18.9° E	120 m	TROPOS	112	cc, pc, s	Dec 2010–Mar 2011
Stockholm, Sweden	59.4° N	18.1° E	16 m	1st	1139	cc, m	Aug 2010–Jun 2014
Warsaw, Poland	52.2° N	21° E	100 m	UW	121	cc, pc, md	Jun 2013–ongoing
R/V *Polarstern*	Atlantic,	North–South		TROPOS			
				OCEANET	193	m, md, pc, s	Oct 2009–ongoing
R/V *Meteor*	Atlantic,	along 15° N		OCEANET	26	md, m, s	Apr 2013–May 2013

ACPD
15, 27943–28004, 2015

Table 2. Overview of aerosol properties as derived within Polly^{NET} by the end of 2014. LR is the Lidar ratio, $Å_\alpha$ the extinction-related Ångström exponent, and δ_{par} the particle linear depolarization ratio at ^{1} = 355 nm, ^{2} = 532 nm. ± indicates standard deviation. E14 = Eyjafjallajökull, PRD = Pearl River Delta, SDZ = Shangdianzi.

Aerosol type	355 nm-LR [sr]	532 nm-LR [sr]	$Å_\alpha$	δ_{par} [%]	Reference
Dust					
Saharan over Portugal	45 ± 11	53 ± 7	0.0 ± 0.2	28 ± 4^2	Preißler et al. (2011)
Saharan near Cape Verde	50–60	50–60	0.1 ± 0.2	–	Kanitz et al. (2013a)
Saharan near Cape Verde	52 ± 2		0.4 ± 0.4	27 ± 2^1	Illingworth et al. (2015)
Saharan over Leipzig	55 ± 6	50 ± 5	0.1 ± 0.4	27 ± 0.04^2	this paper
Asian over Portugal	55 ± 9	46 ± 14	2.0 ± 0.9	–	Preißler et al. (2013b)
Patagonian		42 ± 17		–	Kanitz et al. (2013a)
Polluted Dust					
Saharan over Portugal	52 ± 20	51 ± 11	0.4 ± 1.2	13 ± 6^2	Preißler et al. (2013b)
Saharan over Warsaw	55 ± 20	70 ± 10	0.5 ± 0.1	20 ± 5^2	Janicka et al. (2015)
Saharan over Leipzig	53 ± 3			19 ± 1^1	Illingworth et al. (2015)
Biomass-Burning Aerosol (BBA)					
Amazon (aged)	62 ± 12	64 ± 15	1.2 ± 0.44	2.5 ± 1^1	Baars et al. (2012)
Iberian Peninsula (winter)	51 ± 17	54 ± 25	1.4 ± 0.5	≤ 5^2	Preißler et al. (2013a)
Portuguese (< 2 days)	56 ± 6	56 ± 6	1.5 ± 0.2	5 ± 0.6^2	Pereira et al. (2014)
South Africa	89 ± 20	83 ± 23	1.8 ± 0.5	–	Giannakaki et al. (2015)
North American over Portugal	58 ± 17	56 ± 28	2.2 ± 0.7	2–6	Preißler et al. (2012)
North American over Leipzig	42 ± 6			10 ± 1^1	Illingworth et al. (2015)
North American over Warsaw	75 ± 30	95 ± 25	1.5 ± 0.2	8±5^1 and 8 ± 5^2	Janicka et al. (2015)
Saharan Dust+African BBA Mix					
near Cape Verde	64 ± 8	50 ± 5	0.1 ± 0.3	22 ± 1^1 and 26 ± 1^2	Kanitz et al. (2014b)
West of Africa (8–21° N, 23° W)	61 ± 4	45 ± 11	0.7 ± 0.3	21±2^1	Kanitz et al. (2013a)
in the Caribbean	45 ± 12	45 ± 7	0.1 ± 0.4	20 ± 1^1 and 20 ± 1^2	Kanitz et al. (2014b)
in Amazonia	40–50	60–70	≈ 0	0.04–0.05^1	Ansmann et al. (2009)
Urban					
PRD at Xinken, China		47 ± 6		–	Ansmann et al. (2005)
PRD at Guangzhou, China		48 ± 11		4 ± 4^2	Heese et al. (2015)
Beijing dust influenced		38 ± 7		–	Tesche et al. (2007)
Beijing continental background		25 ± 5		–	Tesche et al. (2007)
SDZ (Beijing plume)		60 ± 20		–	Hänel et al. (2012)
North American over Portugal	46 ± 23	51 ± 25	1.2 ± 1.1	–	Preißler et al. (2013b)
European over Portugal	64 ± 23	76 ± 33	1.2 ± 1.0	–	Preißler et al. (2013b)
European at Leipzig	57 ± 4	52 ± 4	1.4 ± 0.2	3 ± 1^1	Illingworth et al. (2015)
Indian mean	50 ± 23	42 ± 24	1.0 ± 0.8	–	Komppula et al. (2012)
Volcanic Ash					
E14 obs. near. Bremerhaven	55 ± 10	61 ± 1	≈ 1	30–38^1	Kanitz (2012)
E14 obs. in Évora	39 ± 10	34 ± 4	0.7 ± 0.6	–	Sicard et al. (2012)

ACPD
15, 27943–28004, 2015

Table 2. Continued.

Aerosol type	355 nm-LR [sr]	532 nm-LR [sr]	$Å_\alpha$	δ_{par} [%]	Reference
Seasonal analysis					
South Africa Spring	89 ± 21	82 ± 25	1.8 ± 0.9		Giannakaki et al. (2015)
South Africa Summer	57 ± 20	39 ± 18	2.4 ± 0.9		Giannakaki et al. (2015)
South Africa Autumn	59 ± 22	58 ± 26	1.8 ± 0.7		Giannakaki et al. (2015)
South Africa Winter	65 ± 23	60 ± 23	1.8 ± 0.6		Giannakaki et al. (2015)
South Africa Wet	67 ± 26	69 ± 32	2.0 ± 0.8		Giannakaki et al. (2015)
South Africa Dry	67 ± 24	63 ± 24	1.8 ± 0.7		Giannakaki et al. (2015)
India Spring	45 ± 15	36 ± 20	1.1 ± 0.8		Komppula et al. (2012)
India Summer	57 ± 28	53 ± 28	0.7 ± 0.7		Komppula et al. (2012)
India Autumn	77 ± 33	60 ± 41	1.3 ± 1		Komppula et al. (2012)
India Winter	46 ± 19	37 ± 21	1.4 ± 0.7		Komppula et al. (2012)
SDZ, China Spring		58 ± 9			Hänel et al. (2012)
SDZ, China Summer		61 ± 9			Hänel et al. (2012)
SDZ, China Autumn		59 ± 9			Hänel et al. (2012)
SDZ, China Winter		68 ± 11			Hänel et al. (2012)

ACPD
15, 27943–28004, 2015

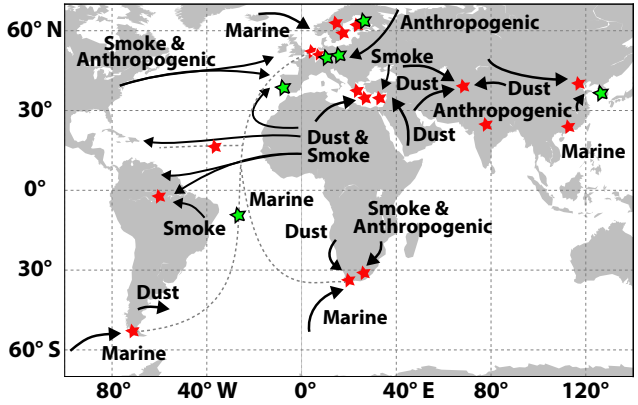

Figure 1. Global map of Polly measurement sites. Green stars mark the six permanent and one shipborne long-term stations while red stars represent temporary measurement locations. Intercontinental aerosol transport regimes are indicated by black arrows.

ACPD
15, 27943–28004, 2015

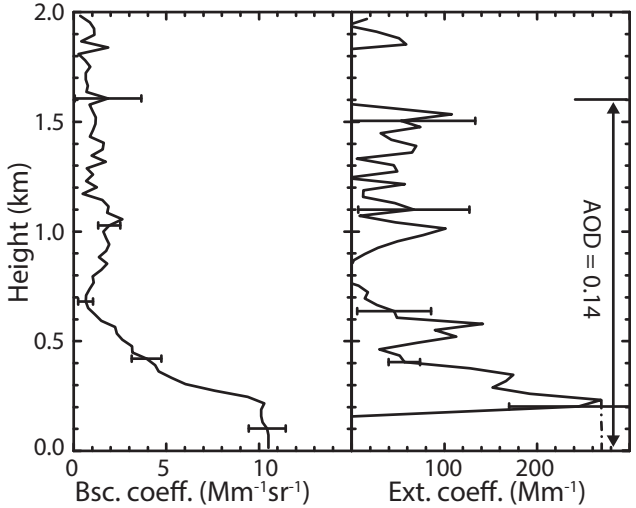

Figure 2. Profiles of **(a)** particle backscatter and **(b)** extinction coefficients at 532 nm measured with the first-generation Polly in Leipzig, Germany on 10 December 2002.

ACPD
15, 27943–28004, 2015

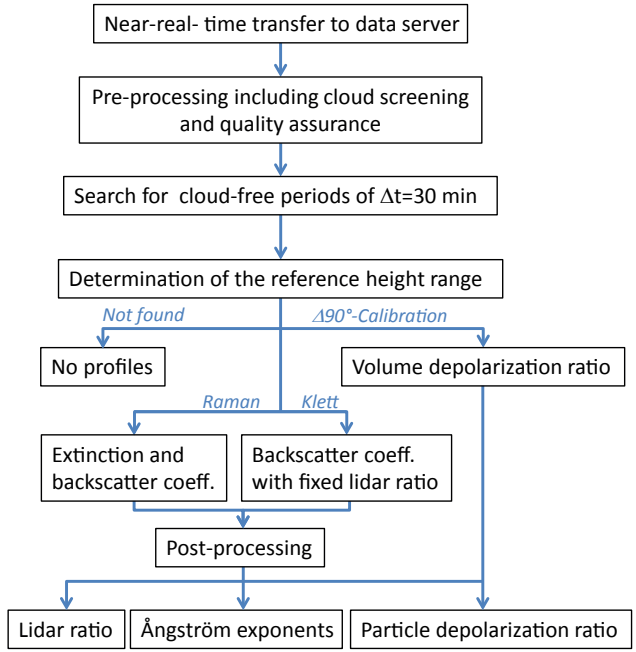

Figure 3. Schematic description of the steps for the automatic data analysis. For details see the text and Appendix A.

ACPD
15, 27943–28004, 2015

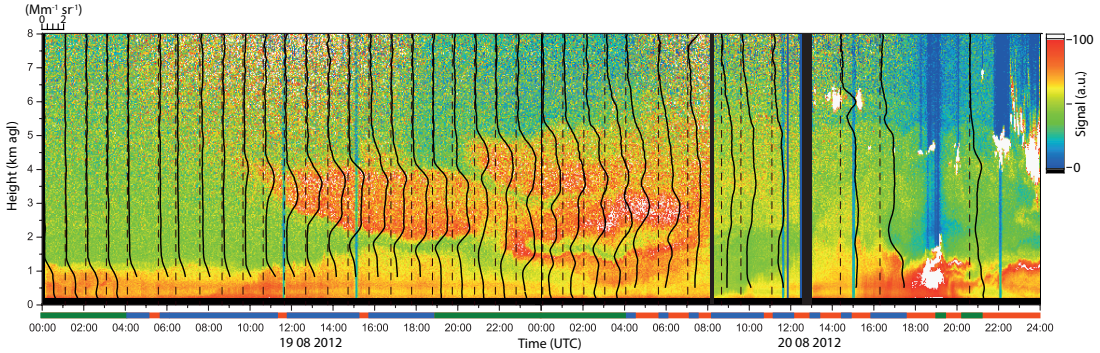

Figure 4. Temporal development of backscatter intensity in terms of range-corrected signal at 532 nm in Leipzig on 19 and 20 August 2012. Corresponding automatically derived particle backscatter coefficient profiles at 532 nm are overlaid in black. The color bar at the bottom shows the retrieval status: green – Raman, blue – Klett, red – no retrieval. A change of neutral-density filters at around 08:15 UTC on 20 August results in a changed backscatter intensity.

ACPD
15, 27943–28004, 2015

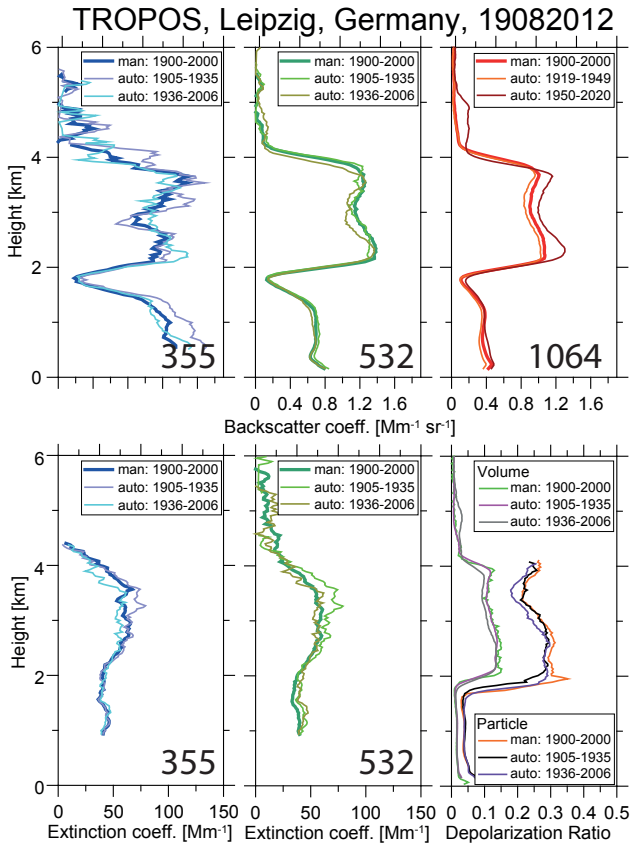

Figure 5. Comparison of manually (man) and automatically (auto) derived optical products for 19 August 2012 between 19:00 and 20:20 UTC. Backscatter coefficient at 355, 532, and 1064 nm (top), extinction coefficient at 355 and 532 nm, and linear polarization ratio at 532 nm is shown.

ACPD
15, 27943–28004, 2015

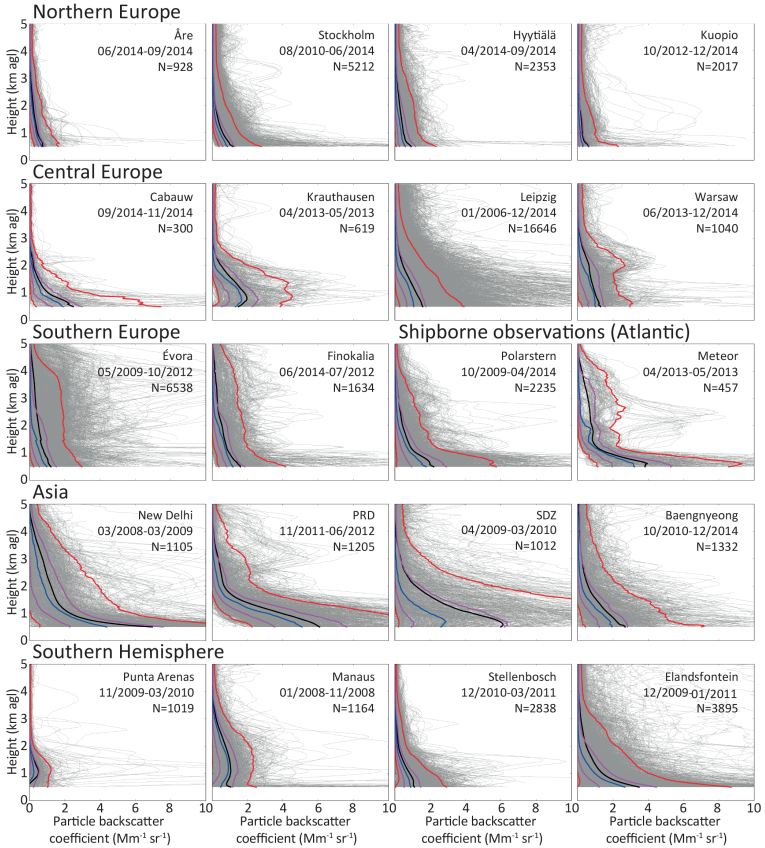

Figure 6. Profiles of 532 nm particle backscatter coefficients at the Polly^{NET} measurement sites. Individual 30 min profiles are shown as thin grey lines. Median (blue), mean (black), 25 and 75 % percentile (purple), and 5 and 95 % percentile (red) profiles are given. The location and number (*N*) of the presented profiles is given in each plot. Details of the specific stations can be found in Table 1.

ACPD
15, 27943–28004, 2015

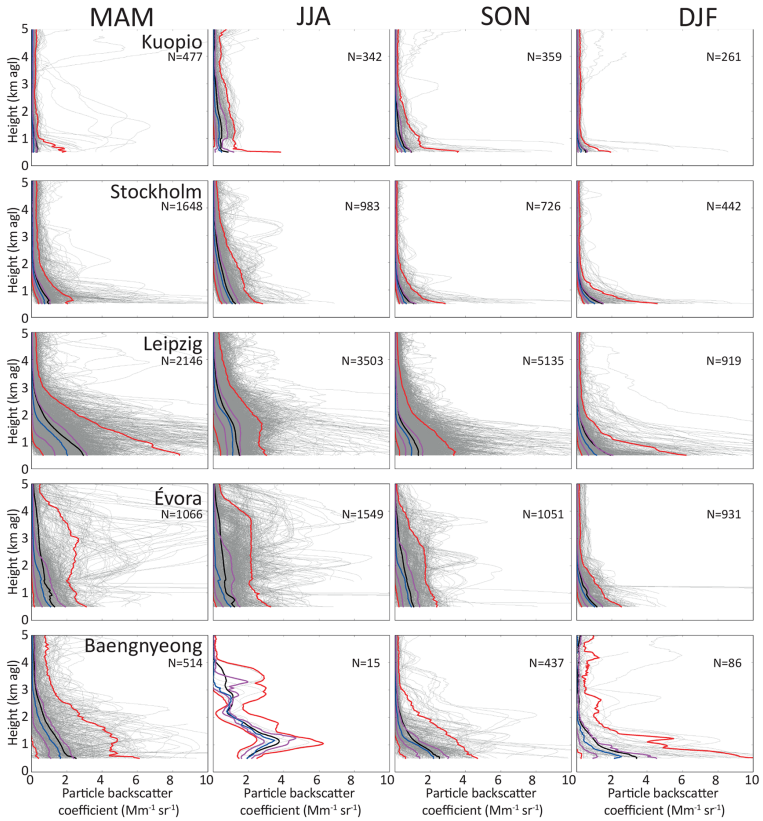

Figure 7. Profiles of 532 nm particle backscatter coefficients determined for spring (MAM), summer (JJA), autumn (SON), and winter period (DJF) from Polly^{NET} measurements. The number (N) of the presented profiles is given in each plot. All profiles are shown by thin grey lines. Median (blue), mean (black), 25 and 75 % percentile (purple) and 5 and 95 % percentile (red) profiles are given. Details of the specific station can be found in Table 1.

ACPD
15, 27943–28004, 2015

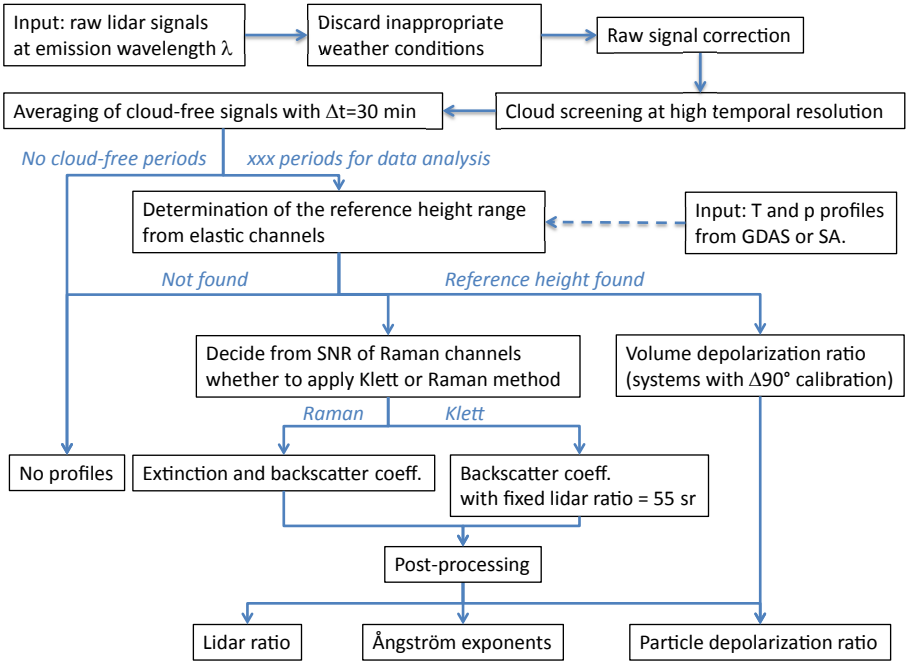

Figure A1. Schematic description of the automatic retrieval in Polly^{NET}. Details are given in the text. GDAS=Global Data Assimilation System, SA = Standard Atmosphere.

ACPD
15, 27943–28004, 2015

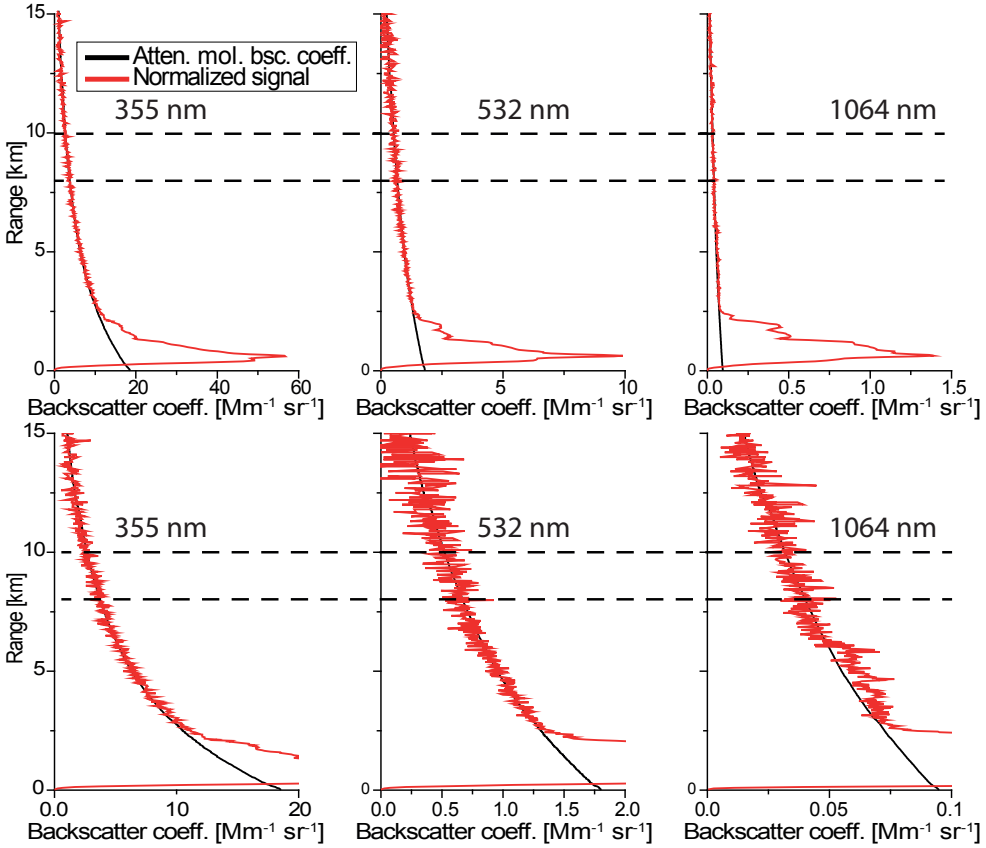

Figure A2. Rayleigh fit (normalized lidar signal) calibrated between 8 and 10 km and profiles of the attenuated molecular backscatter coefficient at 355 (left), 532 nm (center), and 1064 nm (right). *x* axis zoomed in for lower panels.

ACPD
15, 27943–28004, 2015

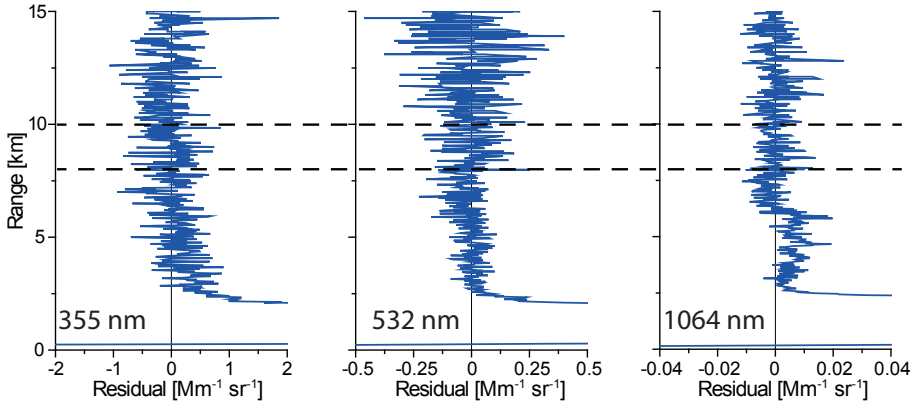

Figure A3. Residual of the Rayleigh fit shown in Fig. A2 for 355 nm (left), 532 nm (center), and 1064 nm (right).

ACPD
15, 27943–28004, 2015